Fall 2011

Antenna design: a crystallographical approach

Luke MacVicker Snow
San Jose State University

ANTENNA DESIGN:
A CRYSTALLOGRAPHICAL APPOACH

A Thesis

Presented to

The Faculty of the Department of Electrical Engineering

San José State University

In Partial Fulfillment

of the Requirements for the Degree

Master of Science

by

Luke M. Snow

December 2011

The Designated Thesis Committee Approves the Thesis Titled

ANTENNA DESIGN:
A CRYSTALLOGRAPHICAL APPOACH

by

Luke M. Snow

APPROVED FOR THE DEPARTMENT OF ELECTRICAL ENGINEERING

SAN JOSÉ STATE UNIVERSITY

December 2011

Dr. Sotoudeh Hamedi-Hagh	Department of Electrical Engineering
Dr. Raymond Kwok	Department of Electrical Engineering
Dr. Masoud Mostafavi	Department of Electrical Engineering

ABSTRACT

ANTENNA DESIGN:
A CRYSTALLOGRAPHICAL APPROACH

by

Luke M. Snow

The goal of this thesis was to design a switched beam antenna by applying the principles of crystallography. The main benefit of this approach is that simple design equations can be derived from crystallography and readily applied to the design of a steerable beam antenna. Before using equations from crystallography in an antenna design, the equations are first verified. One of the best known laws of crystallography, namely Bragg's Law, is verified both by software simulation, and experimentally from the radiation patterns of a prototype antenna.

One set of simulations used to verify Bragg's Law involved varying the angles of incidence while changing the plane spacing accordingly to maintain the diffraction condition. The average deviation between the software simulation and the calculated diffracted peak location was 0.8%, confirming Bragg's Law at radio frequency. A prototype antenna was designed using Bragg's Law, and the peak location was verified experimentally. The antenna was designed for use at around 6 GHz.

Having verified that principles from crystallography can be applied at radio frequencies, a switched beam antenna array was designed. The antenna had three possible directions: forward, and +/- 90 degrees relative to the incident beam. The side lobe level was 15.7 dB, and the half power beam width was 2 to 3 degrees.

ACKNOWLEDGEMENTS

First, I would like to thank my thesis advisor Dr. Ray Kwok not only for providing direction in this work, but also in editing the paper and proposal. Additionally, his advice for measuring the antenna radiation patterns was invaluable. He also aided me in understanding and applying the concepts of crystallography. Without his help, this work would not have been accomplished.

My colleagues at Space Systems Loral were of great assistance as well. Jeffrey Gregory generously helped with the actual data gathering for the antenna radiation patterns, Jason Blonstein for the use of a company network analyzer, Kevin Rudy and Clif Mitchell for the use of the CATR facility and advice in the experimental setup of the antenna measurement.

I would also like to thank my family: Nancy Shull for proofreading this thesis; my father-in-law, William Shull of Zygo Corporation, for providing practical design insights, and use of his machine shop; and especially my wife, for supporting me in my studies. Without her encouragement and assistance my master's degree would have been much longer in coming.

Finally, this work is dedicated to my father, Peter Snow, for always telling his son that he could do "anything you put your mind to."

Table of Contents

List of Tables

List of Figures

1. INTRODUCTION

1.1 Motivation

An important aspect of an antenna's design is its directionality. At some angles an incident signal may be received well (e.g., beams incident on a dipole antenna, and perpendicular to the antenna), while at others it may receive no signal at all (e.g., along the axis of the dipole). It is apparent that an antenna which can change its directionality upon command would be very useful. Such “smart antennas” are used in military, scientific, or commercial settings.

One form of a smart antenna is a “phased array” of radiators. A significant challenge in implementing the phased array is the steering of the beam. To solve this problem, the phases or amplitudes of each radiator must be altered, so that the beam points in a different direction.

To alter the phase of the signal, a component known as a "phase shifter" is used. At higher frequencies of operation, effectively shifting the phase of the transmitted signal becomes more difficult, as tolerances are tighter. The limitations of the phase shifter thus limit the frequency of operation for phased arrays.

Traditionally, antennas with electrically tunable beams make use of both the phase and the amplitude in setting the direction of the beam. If a limitation of an antenna with a steerable beam is the phase shifter, would it be possible to create such an antenna without the use of a phase shifter?

A field which has achieved a considerable amount without the aid of phase information is crystallography. In this field, X-ray diffraction is used as a tool in determining the periodic structure of crystalline materials. Even the "softest" of X-rays propagate at an exceedingly high frequency. It is not possible to measure phase variations at X-ray frequencies, and thus all information gleaned from the techniques of X-ray diffraction rely only on intensity and diffracted angle. This the well known "phase problem" of crystallography [1].

Given the established state of the field of crystallography, there are doubtless useful parallels that can be drawn with phased array antenna design. In particular, phased arrays might effectively be designed for operation at high frequencies without the use of phase shifting, just as the study of crystal structure has progressed without knowledge of phase information.

1.2 Organization

This paper is organized as follows: Chapter 2 gives a literature review, exploring work similar to that presented here, as well as a brief history of the pertinent disciplines. Chapter 3 gives the methodology employed: the steps followed and tools used to explore the ideas. Chapter 4 presents the theory, both qualitatively and quantitatively, and the parallels between crystallography and antenna design. Chapter 5 lays out the experimental setups. Chapter 6 gives the results, along with discussion. Chapter 7 is a conclusion and exploration of further work to be done.

2. LITERATURE REVIEW

2.1 Crystallography

The field of crystallography has been around since before the use of X-rays to study crystal structures. However, the use of X-ray diffraction to study crystals gained popularity with the discovery of Bragg's Law [2]. Bragg's Law provided a valuable theoretical tool for visualizing how X-rays are diffracted from a crystal. In this formulation, X-rays can be seen as "reflecting" off planes of atoms within a crystal. The angle at which the X-rays are diffracted, relative to the incident beam, along with a knowledge of the wavelength of the X-ray, gives the spacing between the planes. The plane spacing, then, gives valuable information about the crystal structure.

Bragg's Law determines only the direction of the diffracted beam as it is scattered off of a crystal; it does not provide information about the intensity of the diffracted beam. There are numerous other factors that affect the intensity of the beam. The structure factor, for example, takes into account the affect of the specific atoms in the crystal. The Scherrer equation [3] describes the affect of crystal size. The absorption of X-rays by the crystal also affects the intensity.

There are numerous laws and techniques that have been developed in the field of crystallography. While the methods of X-ray diffraction have been developed for light of short wavelengths interacting with microscopic atoms, it is instructive to consider what information might be gained from a parallel with centimeter scale Radio Frequency (RF) wavelengths and macroscopic objects on the same scale.

2.2 Photonic Crystals

The idea that the physics of interaction between electromagnetic radiation and atoms, or electron energy states in a lattice can be observed analogously on a larger scale is by no means unique. In his landmark paper [4], Yablonovitch began the study of photonic band gap materials, relating electronic and electromagnetic band gaps. Using the scale invariance of electricity and magnetism, that is, the notion that Maxwell's equations are equally valid at all scales, the properties of photonic band-gap materials would later be studied using centimeter-scale models.

On a larger scale, a photonic crystal is a regular array of objects, such as a metal or a dielectric, used to scatter light in a desired fashion. The photonic crystal has properties similar to atomic crystals. It can form a band-gap [5], or it can diffract light. Some more recent potential applications of photonic crystals include a beam focusing antenna substrate [6], 4-port switch [7], and band pass or band block filters [8]. All of these applications use the band-gap property of photonic crystals, where some frequencies of light are allowed to travel through the crystal and others are blocked. As an antenna substrate, the light radiated by the antenna cannot radiate into the photonic crystal. As a switch, the photonic lattice is constructed inside of a waveguide and is altered to focus the incident light into a given port. As a band pass structure, the photonic crystal is inside a waveguide and some frequencies of light are allowed to pass through the waveguide.

In the work at hand, a photonic crystal is used not in the band-gap regime, but in the permissible band, i.e., the in-band energy states where Bragg scattering is possible.

2.3 Antenna Theory

The antenna plays a fundamental part in communication systems. It is the interface between the transceiver and the free space through which the signal propagates. The types of antennas are as varied as the types of applications in which they are used. A simple ground plane monopole antenna is used for reception of signals from many directions; more complex antennas with directionality that can be changed are of use in radar; a high-gain TV dish is adjusted once to focus on a satellite signal; smart antennas can change the direction of reception based on the signal which is being received; etc.

The analysis and design of the antenna presented in this paper appear to be unique. While Bragg's Law (and other principles of crystallography presented herein) has been used in a variety of contexts other than solid state physics, such as acousto-optics [9], photonic crystals [10], or even at radio frequency [11], it does not appear to have been used as an analysis tool for antenna design.

2.3.1 Smart Antenna

There are two broad categories into which most smart antennas fit: adaptive arrays and switched beam arrays. The adaptive array is a more complex system, but has the advantage that the main beam can be formed to aim in most any direction. The switched beam array is simpler, but only a predetermined set of directions is possible.

The switched beam design presented in this paper also appears to be unique. While the idea of changing the active antenna elements rather than using a phase shifting network for beam steering is not unique [12], the particular antenna geometry and the use of the Ewald sphere to determine its possible beams is novel.

2.4 Geometrical Theory of Diffraction

Classic Geometric Optics consists of three laws: rectilinear propagation, reflection, and refraction. With these laws, light is treated as a ray which travels in a straight line, can be reflected off a surface, and can be bent when transitioning between different materials. Missing from this list of laws is an account of how light diffracts. With the Geometrical Theory of Diffraction (GTD), J.B. Keller [13] added an explanation of diffraction to Geometric Optics.

The basic functionality of the GTD explains how light diffracts off certain objects, such as edges, tips, or curved surfaces [14], [15]. In the work at hand, the earlier antenna models were improved by eliminating sharp tips from part of the design, as the sharp tips in the design would introduce undesired tip diffraction.

2.5 Conclusion

The antenna presented in this paper appears to be novel, and is cross-disciplinary in nature, pulling concepts from crystallography to design an antenna. The GTD is used to improve the antenna design.

3. METHOD

3.1 Work Flow

In all of the concepts discussed, there are two possible flows to follow, given in Figs. 3.1 and 3.2. Most of the concepts discussed were verified using the flow diagram of Fig. 3.1. In all of the concepts, some crystallographic law was discussed, and it was argued that the law was valid also for radio frequencies. A design isolating the necessary parameters was then created with software, and the concept was verified.

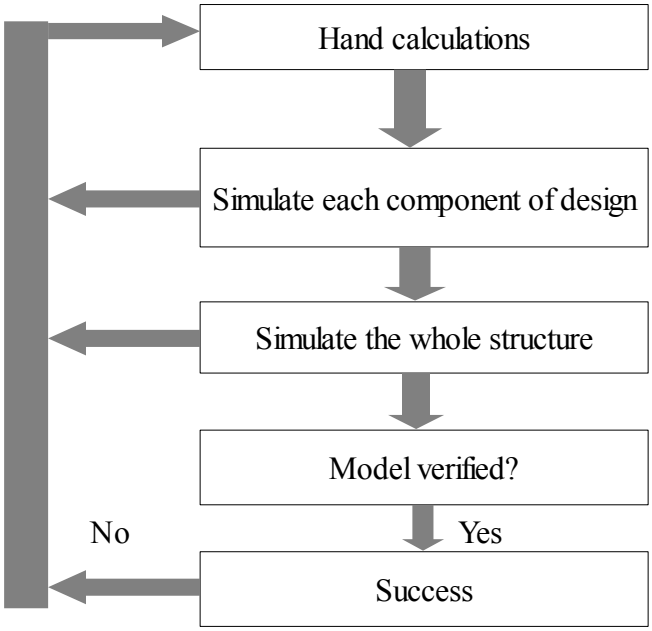

Figure 3.1 - Design flow for quantities verified only in software simulation

The other flowchart followed was that of Fig. 3.2. One particular concept was verified: that of Bragg's Law of Diffraction. First, the structure based on hand calculations was simulated in software. The structure was then fabricated, and measurements were made to verify the law.

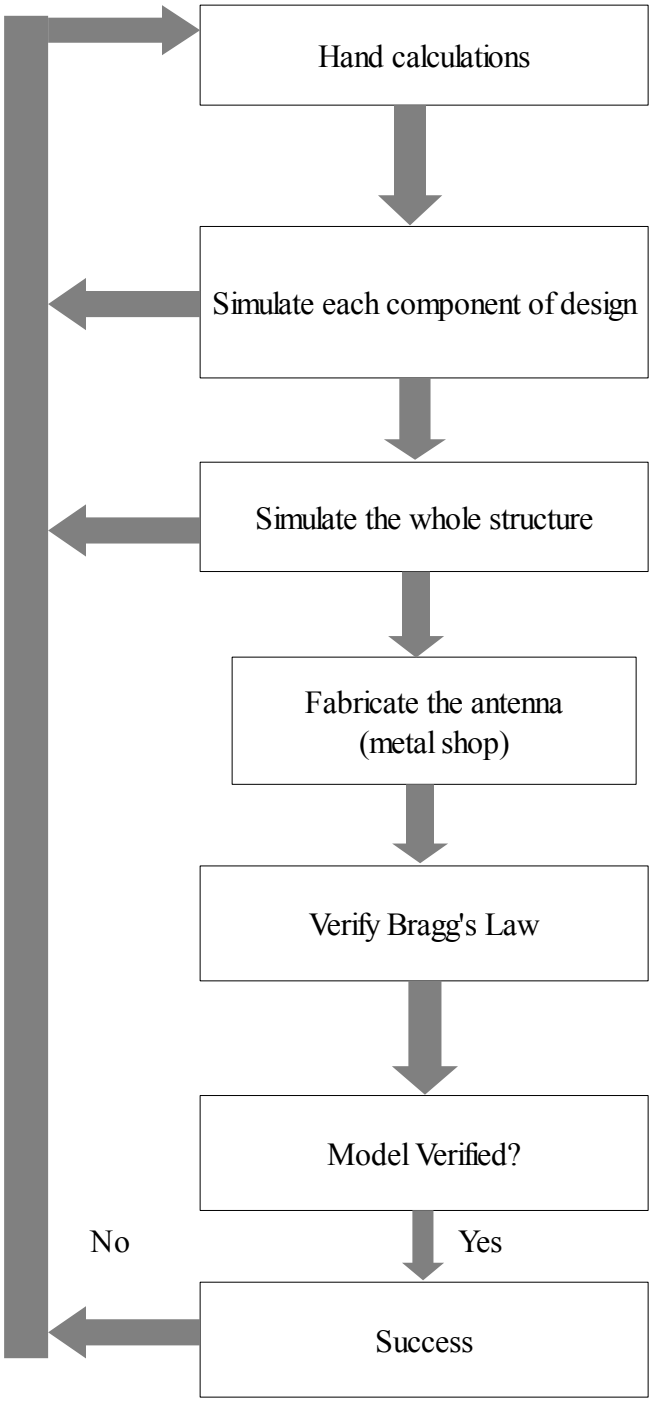

Figure 3.2 - Flow chart for the antenna design process

In both charts, the design flow parallels the organization of the thesis: hand calculations (theoretical); simulation (experimental), verification (discussion and results).

3.2 Software

The designs simulated throughout this paper make use of the Ansoft High Frequency Structure Simulator (HFSS) software. HFSS is a three-dimensional full wave solver that uses the finite element method. For a more detailed discussion of the software and its use, refer to the appendix at the end of the paper.

4. THEORETICAL

4.1 A Correspondence

In what follows, connections will be made between the fields of crystallography and antenna design. The first comparisons will be qualitative, followed by quantitative descriptions.

4.2 Crystallography Basics

It is appropriate at this point to provide a succinct definition of the term *crystal*. This term is best broken into two parts: the lattice and the basis. The lattice of a crystal is made up of a basic unit cell. The unit cell is a basic geometric shape, such as a cube or a parallelepiped; it is the building block of the lattice. If unit cells were stacked indefinitely in every direction, the lattice would be obtained. In crystallographic theory, all crystals can be represented by the 14 Bravais Lattices.

The crystal does not only consist of a lattice, but it must also have a basis, or collection, of atoms associated with each lattice point (the lattice point being the vertices of the unit cell; e.g., a cube has 8 lattice points). The simplest basis would be a single atom, located at a lattice point. Of course, there can be multiple atoms associated with each lattice point, making for a more complicated structure.

A *crystal*, then, is defined as a lattice-basis combination. If the lattice is specified, and the basis is specified, then the crystal is completely known.

4.2.1 The Classic X-Ray Diffraction Setup

In the classic X-ray diffraction experiment, there are three basic components, as shown in Fig. 4.1 below. There is the X-ray source, the sample, and the detector. The X-ray source irradiates the sample, and the sample diffracts the energy into various directions. The detector measures the intensity of the radiation at an angle 2θ (or perhaps θ depending on the setup). A typical experimental setup, for example, would consist of a detector that rotates at a constant angular velocity. The sample remains fixed and the detector rotates in the plane of the paper of Fig. 4.1, while X-rays are continuously incident upon the sample. This is known as the Bragg-Brentano Geometry.

An example of data of this sort is given in Fig. 4.2, below. The radiation used was Cu Kα (copper, Kα radiation, $\lambda \sim .154$ nm). A powdered sample of Na Cl was used. A detector registering counts of radiation was used. A prominent feature of this graph is the relatively large peak at an angle 2θ of 32 degrees.

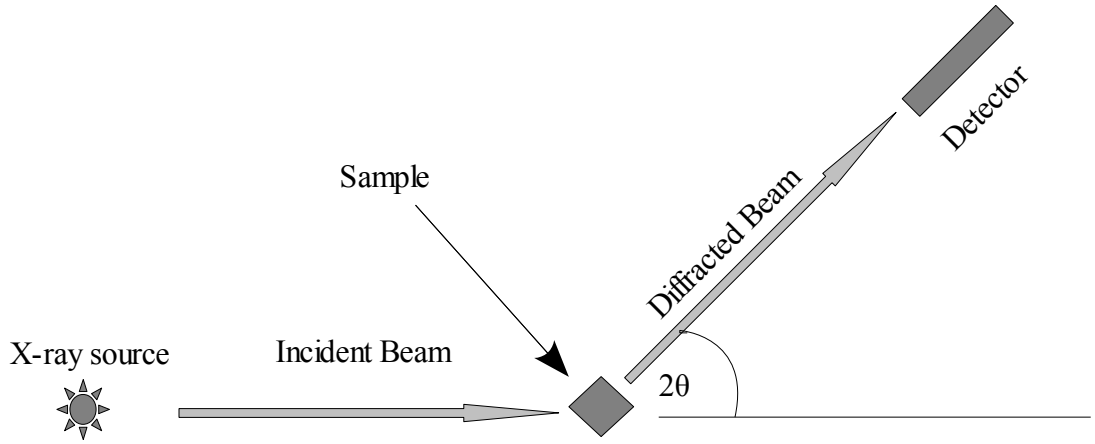

Figure 4.1 - The classic X-ray diffraction experiment

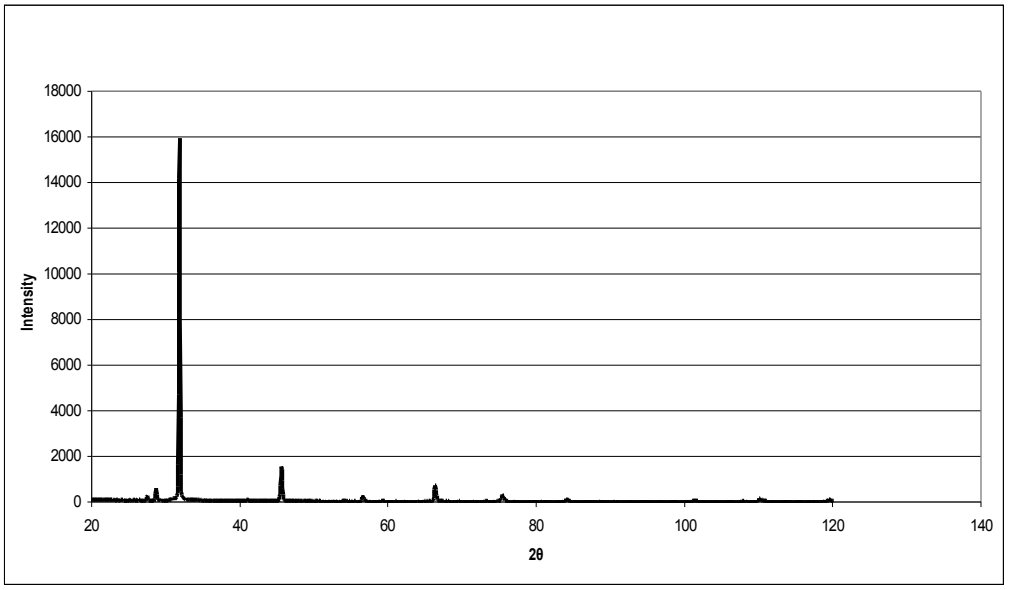

Figure 4.2 - Actual data from an X-ray diffraction experiment

There are, of course, variations for each of the basic components listed above. The X-ray source may have different wavelengths; the sample could be a single crystal, or a powder; the detector could be a photo-multiplier tube, or even just a special photograph. A "Laue photograph" is given in Fig. 4.3. In this setup, a single crystal is held fixed and irradiated. The diffracted beam is then scattered in various directions, some of which fall onto a special photograph that is sensitive to X-rays. As shall be seen, each of the above setups has similarites to a typical antenna setup.

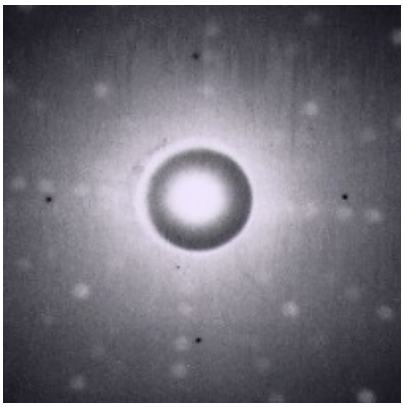

Figure 4.3 - A Laue photograph of silicon

4.2.2 The Geometry of an Antenna Setup

Similar to the experimental setups discussed above, a typical antenna setup can be viewed as having three basic parts as well: a stimulus, a transmitting antenna, and a receiving antenna. The stimulus would be some feeding structure for the antenna (generally a waveguide). The transmitting and receiving antennas could be horns, dipole antennas, or phased arrays. They need not be of similar geometry, either.

4.2.3 A Relation of Terms

At first look there may not be much similarity between an X-ray diffraction experiment and an antenna setup. The goals in each situation are different. In an X-ray diffraction experiment, one observes the X-rays diffracted by a crystal in hopes of finding information about the sample. The sample is the unknown object of interest. An antenna, on the other hand, is of known geometry. The antenna is designed to radiate radio frequency light in a desired direction.

While the goals in each situation are different, there are many similarities. The waveguide stimulus acts like the X-ray source, the transmitting antenna is like the sample, and the receiving antenna is analogous to the detector in the X-ray diffraction experiment. In fact, the sample in an X-ray diffraction experiment can be viewed as a scaled-down version of an antenna array at an extremely high frequency (short wave-length).

In the X-ray diffraction experiment, it is desired that the light incident on the sample be a plane wave. Additionally, the sample consists of a crystal having many atoms, each radiating a portion of the light. It is desired that the diffracted light travel a distance that is large compared to the inter-atomic spacing in the crystal, such that the whole crystal can be treated as a point source.

In antenna design terminology, a plane wave in free space is a transverse electro-magnetic (TEM) mode; that is, the electric field, magnetic field, and direction of

propagation are mutually orthogonal. The atoms in the crystal then become the individual antennas which comprise the antenna array. The condition that the diffracted light travels "far" becomes the far field requirement for measuring an antenna. This information is summarized in Table 4.1

Table 4.1 - The analogous terms of crystallography and antenna design

X-ray diffraction	Antenna design
X-ray source	feed
plane wave	TEM mode
crystal	antenna array
atom	antenna element
detector	receiving antenna
large detector distance	far field

The desirable properties of the experimental setups corresponding to the data of Figs. 4.2 and 4.3 need further investigation. The data of Fig. 4.2 can be recast as a "radiation pattern," as shown in Fig. 4.4.

This radiation pattern has a very desirable characteristic – it is highly directional. The photograph of Fig. 4.3, having numerous small "dots," shows this property in a different manner; the brightness of the dots representing the intensity, rather than a number assigned to the amount of counts.

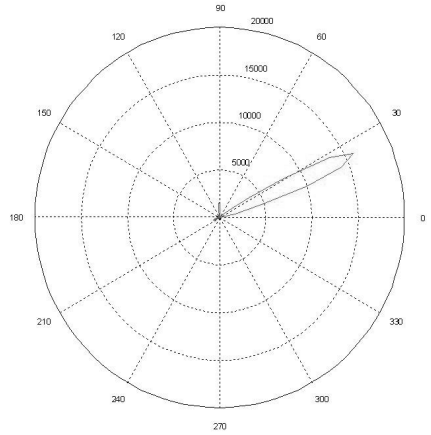

Figure 4.4 - Powder diffraction data viewed as a radiation pattern

4.3 Crystallographic Quantities

So far the discussion of the similarities between X-ray crystallography and antenna design has been qualitative. At this point, a quantitative description of various physical laws is given.

4.3.1 The Bragg Law

When X-rays are incident on a crystal, each atom acts like a point source, diffracting the beam. Since the crystal has a regular repeating structure, the diffracted beam exits the crystal in a pattern that reflects the crystal structure. It was first proposed by father-son team WL Bragg and WH Bragg [2] that the diffraction condition is satisfied when X-rays of a given wavelength are incident on planes of atoms in a prescribed manner. In Fig. 4.5, each horizontal line represents a plane of atoms, spaced at a distance "d." The wavelength of the incident and diffracted X-radiation are given by λ.

The Bragg condition for diffraction is satisfied when the two incident beams interfere constructively. In other words, the path length difference between beam ACD and the beam incident at B must be an integral number of wavelengths. Some simple trigonometry shows that this can be written mathematically as

$$m\lambda = 2d\sin\theta \quad (4.1).$$

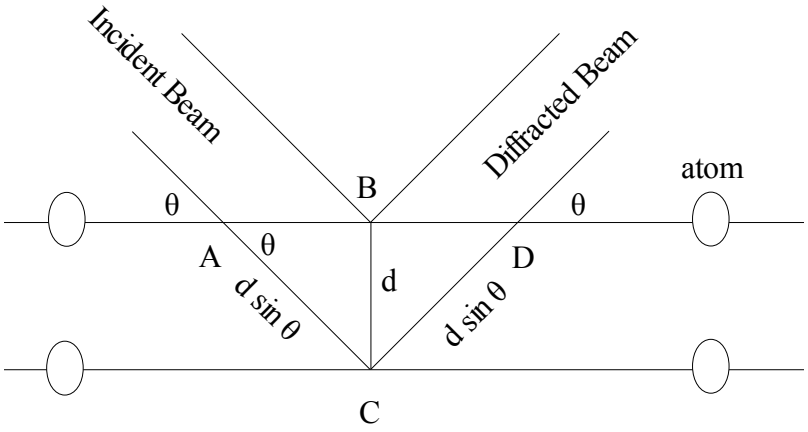

Figure 4.5 - The Bragg condition for diffraction

As Fig. 4.5 suggests, the Bragg condition for diffraction is very much similar in appearance to a reflection of light from a mirror in optics. This similarity is the reason that a Bragg diffraction is sometimes referred to as a "Bragg Reflection." Note, however, that the angle in optics is measured relative to the normal, while the angle in Bragg diffraction is measured relative to the plane of atoms.

The Bragg Law, when solved for θ, also yields information about how the location of the peak changes with variation in frequency. If the wavelength is replaced with c / f and θ is isolated, the following expression is obtained:

$$\theta = \sin^{-1}\left(\frac{c}{2 d f}\right) \quad (4.2).$$

4.3.2 The Scherrer Equation

As discussed in 4.2.1 above, a beam of X-rays incident on a powdered crystal sample will form a diffraction pattern. The angles and intensities of the peaks (see Fig. 4.2) are determined by the structure of the crystal.

However, there is more information that can be gleaned from such data. The width of the peaks can be used [3] to determine the size of the crystallites in the powdered sample. The Scherrer equation, relating peak width to crystallite size, is given by

$$B = \frac{K \lambda}{L \cos\theta} \quad (4.3),$$

where B is the full width at half maximum (FWHM), K is a dimensionless factor determined by the crystallite shape, λ is the wavelength, L is the edge of a cubic crystal, and θ is the angle of incidence. This equation can be recast in frequency dependent form by substituting c / f for λ.

This equation is of restricted generality, derived for the case of a cubic crystal of atoms, and is valid for crystals of a size less than about 1000 unit cells along a given

edge. Additionally, it is questionable as to whether or not this equation holds for the case of a macroscopic antenna design.

The above equation was derived assuming the following:

1. The intensity of light scattered from a single crystal is given by

$$I = I_e F^2 \frac{\sin^2(\pi/\lambda)(\vec{s}-\vec{s}_0)\cdot N_1\vec{a}_1}{\sin^2(\pi/\lambda)(\vec{s}-\vec{s}_0)\cdot\vec{a}_1} \frac{\sin^2(\pi/\lambda)(\vec{s}-\vec{s}_0)\cdot N_2\vec{a}_2}{\sin^2(\pi/\lambda)(\vec{s}-\vec{s}_0)\cdot\vec{a}_2} \frac{\sin^2(\pi/\lambda)(\vec{s}-\vec{s}_0)\cdot N_3\vec{a}_3}{\sin^2(\pi/\lambda)(\vec{s}-\vec{s}_0)\cdot\vec{a}_3} \quad (4.4).$$

2. The Bragg Law holds.

It will now be shown that both of these criteria are satisfied for this case. The analogous form of Equation 4.4 for antenna design is known as the Array Factor [16]. For a two-dimensional array, it is given by

$$AF_n(\theta,\phi) = \frac{1}{M} \frac{\sin(\tfrac{1}{2} M \psi_x)}{\sin \tfrac{1}{2}\psi_x} \frac{1}{N} \frac{\sin(\tfrac{1}{2} M \psi_y)}{\sin \tfrac{1}{2}\psi_y} \quad (4.5).$$

In this equation, M and N are the overall length of the array in the x- and y- directions. These correspond to $N_i a_i$ above. The remaining term is given by

$$\psi_i = k\, d_i \sin\theta\cos\phi + \beta_i \quad (4.6),$$

where k is the wave number, d_i is the spacing of the radiators (or a_i above), and β_i is the phase needed to obtain a peak in the (θ,ϕ) direction. In the typical antenna design scenario, ψ_i is determined in the antenna design. For the case of X-ray diffraction, the phase cannot be set, and thus ψ_i must be determined by a Bragg reflection, given by $(\pi/\lambda)(\mathbf{s}-\mathbf{s_0})$. The term $(\mathbf{s}-\mathbf{s_0})$ is the difference between the incident

wave vector and the diffracted wave vector in the Bragg condition. The I_e term contains constants and other angular terms, and F^2 is the structure factor.

There are some other discrepancies between these two equations: in the formula for the intensity, the term involves sine squared terms and the array factor does not. This is explained simply by the fact that the intensity involves energy and the array factor applies to the electric field. The electric field is squared to give intensity. Also, the intensity equation involves three terms, while the array factor involves two. The intensity equation can easily be reduced to two terms by requiring that the dot product of the diffracted beam with $\vec{a}_3$ direction is zero; then, via L'Hospital's rule the third term reduces to unity.

As for the Bragg Law's applicability at radio frequency, it is verified both in an HFSS simulation, and in an actual antenna design in the experimental section below.

4.3.2.1 Effect of Crystal Size

As mentioned above, the factor L in Equation 4.3 is the edge length of the crystal, and is given by $N_1 a_1$, where a_1 is the distance between individual atoms. If all of the other quantities in the equation are held fixed except for N, it is seen that the peak width has a 1/N dependence, and the factor K (determined by crystal shape) may be determined. To verify this dependence is a simple matter, only the crystal size N needs to be varied. This will be verified in simulation in Chapter 5.

4.3.2.2 Effect of Angle

The effect of angle on the peak width is not so easily verified, because the crystal size cannot be held constant while the angle is varied. If the angle is varied then the conditions for diffraction change, as dictated by the Bragg Law. As angle changes, so also must the crystal edge length. The change in dimensions of the crystal are given by the Bragg Law as follows: solving the Bragg equation for atom spacing gives:

$$d = \frac{\lambda}{2\sin\theta} \quad (4.7).$$

Multiplying this result by N and then substituting this into Equation 4.3 for L, the following is obtained:

$$B = \frac{K\lambda}{N\lambda/(2\sin\theta)\cos\theta} = \frac{2K}{N}\tan\theta \quad (4.8).$$

In this equation then, K and N can be held fixed – the crystal size (in number of atoms, N) simply doesn't change, and the angle can be varied. The inter atomic spacing in the crystal is varied to maintain the diffraction condition, and the peak width should vary with tangent θ only.

4.3.3 Absorption

A common interaction between matter and electromagnetic radiation is that of absorption; that is, the absorption of light as it passes through a material. Materials react differently to different wavelengths of light. For example, visible light, or RF for that matter, reflects off of metals. Gamma rays, on the other hand, will pass through a metal.

When X-rays interact with crystals, some of the radiation is absorbed by the crystal. The law describing this effect is exponential:

$$I = I_o e^{-\mu \Delta t} \quad (4.9)$$

where I_O is the initial intensity before impinging on the material, μ is the absorption coefficient, and Δt the thickness of the material. Note that this thickness is the thickness of material actually traveled through. The radiation may be completely absorbed, in which case the thickness isn't necessarily the whole length of the material.

For the case of diffraction, in which the material is incident on the material at an angle θ, Equation 4.9 becomes

$$I = I_o e^{\frac{-\mu \Delta t}{\cos\theta}} \quad (4.10).$$

This accounts for the increased distance that diffracted radiation travels as it moves through the crystal.

4.3.4 The Structure Factor

If Bragg's Law were the only factor to consider in determining a diffracted peak's location and intensity, the study of crystallography would be rather dull indeed. All peaks would have different locations, but would radiate at the same intensity.

Thankfully this is not the case. There are almost limitless possibilities. Not only are different crystal lattices possible, but a crystal can consist of different atoms. The

structure factor is the mathematical starting point for predicting the intensity of a peak relative to other peaks.

The structure factor is given by:

$$F = \sum_n f_n e^{i\vec{\Delta k}\cdot r_n} \quad (4.11),$$

where n is the number of atoms in the basis; f_n is the scattering factor, a measure of how well the atom scatters light; r_n corresponds to the position of the atom within the unit cell; and **Δk** is the vector describing the Bragg condition.

4.3.4.1 Post Diameter

So far, Bragg's Law has been used to find the direction of a desired intensity maximum based on the spacing of planes of posts. Other than the spacing of the posts, the next most obvious parameter to control is the diameter of the posts. Intuitively, a larger object will more effectively scatter light. Thus one would expect that the post diameter would effect how well each post scatters light. The analogous term from crystallography, mentioned above, is the scattering factor f_n. As the post diameter is increased, so is the scattering factor. If the post is made small, so is the scattering factor. In the limiting case, as the diameter becomes vanishingly small the scattering factor approaches zero.

4.3.4.2 Dielectric

The scattering factor f is a measure of how well an atom (or post) scatters light incident upon it. If the post is made of metal it scatters light effectively, as the RF beam

cannot penetrate deeply into the metal. However, if the post is made of dielectric, the RF beam may travel through the post. Once again, it would be expected that the dielectric is in some way related to the scattering factor. This was generally found to be the case. Interestingly, the case is not as clear cut as with post diameter. The increase in scattering power does not appear to be monotonic with increasing dielectric strength.

It was discovered that the main beam was not always split in proportion between the main beam and the undiffracted beam. In a radiation pattern, the energy must be divided into various directions. Furthermore, if the radiation pattern is more intense in one direction it must be less intense in another direction [16]. Stated differently, the radiation pattern can be normalized relative to the main beam. If the antenna is changed, the main beam may become more or less intense.

This concept may be applied to develop a measure of how much a structure is performing like a crystal. In a perfect crystal, there would be only diffracted beam and undiffracted beam. In this case, as one beam increased, the other would decrease, and in proportion. Thus, the average of the two beams would remain the same. If the average remains constant, the radiation pattern is divided between only those two directions, while if it decreases, "parasitic beams" or "side-lobes" are increasing. If the average is increasing, the parasitics are decreasing.

A possible "optimal design" might consist of a structure for which this average is a maximum, since this would indicate the least possible intensity of side lobes. For

Bragg diffractions it would be desired that this optimized design would occur when the Bragg diffraction is the largest.

4.4 Related Antenna Design Parameters

The above crystallographic quantities can be related to familiar antenna design quantities. To begin with, the directionality of the antenna of interest is determined by Bragg's Law. Its Half-Power Beam Width ("HPBW"), or FWHM, is given by the Scherrer equation, which accounts for the number of posts and the angle of diffraction.

In antenna array design, the overall radiation pattern is defined by pattern multiplication, which consists of multiplying the Array Factor (AF) by the field of a single radiating element [16]. In the above discussion, the single radiating element corresponds to the structure factor and the array factor corresponds to the pattern due to the lattice of the crystal.

The characteristics of the single radiating elements, or posts, can be compared to the atomic scattering factor. Both the metal post diameter and relative dielectric strength can be varied in simulation to observe their effects on the radiation pattern.

4.5 Prototype Design Considerations

As mentioned above, there are three parts to the antenna: the stimulus, the antenna, and the detector antenna. In this section, a design for the stimulus and the antenna will be considered. First, the antenna will be designed, and then a suitable stimulus will be devised.

The antenna, based on the discussion so far, should be some kind of crystal-like shape; that is, it should have a unit cell that regularly repeats itself. As discussed in Section 4.3.2 above, for the intensity Equation 4.4 to reduce down to the 2D array factor of antenna array design, the diffracted beam must be perpendicular to one of the directions of the crystal lattice. This is the equivalent of a simplified form of diffraction from a crystal: the two dimensional case, illustrated in Fig. 4.6. The incident plane wave **k**, as shown, has its electric field component perpendicular to the plane of the page (call this the z direction), as does the diffracted beam **k'**.

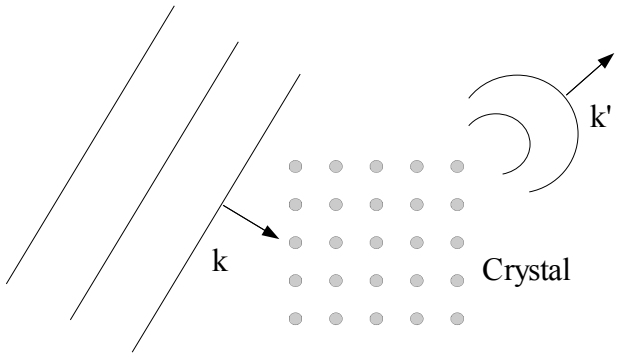

Figure 4.6 - A two-dimensional diffraction experiment

There are a two important points to draw from Fig. 4.6:

1. The plane wave is transverse electromagnetic.
2. The cross section of the crystal is invariant in the z direction.

To fulfill the first requirement, a waveguide must be used that will support a transverse electromagnetic mode (hereafter TEM). The waveguide must also be able to fit the crystal inside of it. To fulfill the second requirement, the "atoms" of the crystal must be

cylindrical posts. The solution becomes apparent: the antenna must be a parallel plate waveguide (this supports a TEM mode) with a regular array of posts between the plates. The solution is shown in Fig. 4.7. Note that the crystal is rotated with respect to the parallel plates to accommodate a TEM wave that is incident at an angle θ to the crystal.

For quantities that were verified with only software simulations, this model is sufficient; in HFSS, a wave port can be assigned to one of the sides of the parallel plate waveguide, and that is all that is needed.

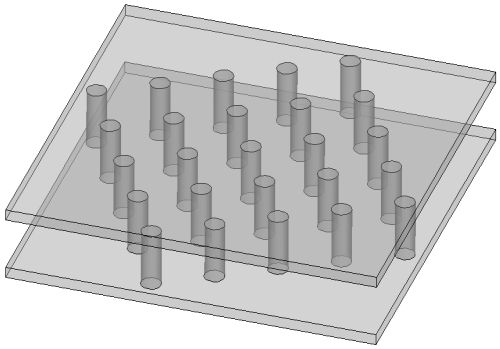

Figure 4.7 - The antenna section

For the experimental verification of Bragg's Law, however, an appropriate feed section must be assigned. The feed must create a plane wave (or something close to it), and it must, like the cross-section of the crystal, be invariant in the z direction so that it transitions into the TEM mode of the parallel plate waveguide seamlessly. A horn is a natural choice, and for the current geometry an H-plane horn must be used. Since signals are typically injected via coax, a waveguide to coax adapter must be used, and that will lead into the horn section.

Now that the necessary sections have been identified, the design particulars can be found for the design verifying Bragg scattering.

4.5.1 The Waveguide Section

The rectangular waveguide section was designed to accomodate a 6GHz TE wave, while also having an inexpensive, commonly available size. The cutoff frequency for a given mode is given by [17]

$$f_{Cmn} = \frac{c}{2}\sqrt{\left(\frac{m}{a}\right)^2 + \left(\frac{n}{b}\right)^2} \quad (4.12).$$

Thus, the TE10 cutoff is

$$f_{C10} = \frac{c}{2a} \quad (4.13)$$

while the next higher mode, TE11, is given by

$$f_{C11} = \frac{c}{2}\sqrt{\left(\frac{1}{a}\right)^2 + \left(\frac{1}{b}\right)^2} \quad (4.14).$$

For operation in the neighborhood of 6GHz, a cross-sectional dimension of 1" x 1.5" was chosen for the outer diameter, while the inner diameter measured 1/8 inch less on each wall. The frequency response for this section is that of a high-pass filter, as shown in Fig. 4.8.

As can be seen in Fig. 4.8, the frequency response of the waveguide is almost unity at 6GHz. Also, the next mode (TE11) is at about 9 GHz, which guarantees that only the TE10 mode will progagate. A summary of this information is given in Table 4.2.

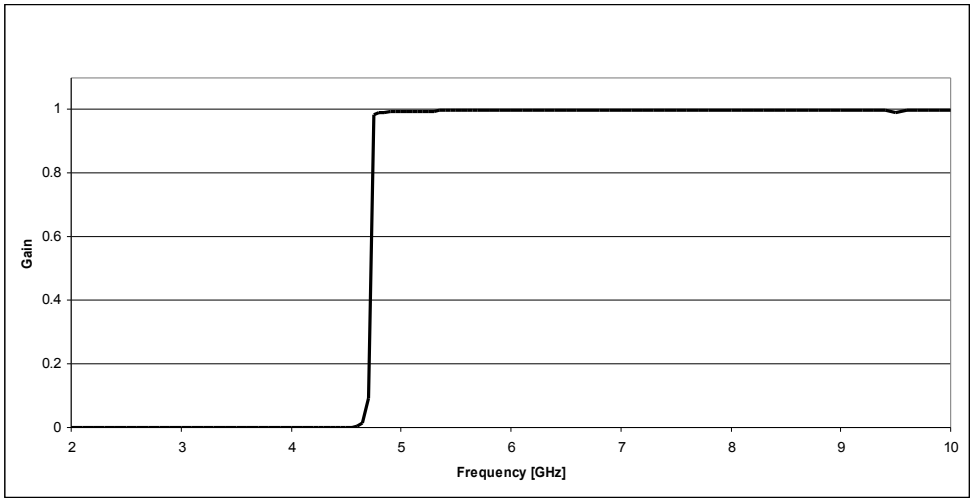

Figure 4.8 - Simulation of frequency response of the waveguide section

Table 4.2 - A summary of the waveguide feed specifications

Parameter	Value
OD	1.5" x 1.0"
ID	1.25" x 0.75"
f_{C10}	4.72 GHz
f_{c11}	9.17 GHz
Length	12"
Feed to center-pin	0.5"

4.5.2 The H-Plane Horn Section

The H-plane horn section was designed to give the minimum phase variation across the wavefront, while also having a pattern that could fit onto a cheap, readily available size of sheet aluminum (3' x 2' x 0.020"). The pertinent design equation is the

maximum phase variation [16], given by

$$\Delta\phi\big|_{max} = k\,\delta(y')\big|_{y'=b_1/2} = \frac{k(b_1/2)^2}{2\rho_1} \quad (4.15)$$

where δ is a function of path length difference across the face of the horn, and multiplication by the wave number "k" gives the actual phase variation; b_1 is the length of the opening, and ρ_1 is the distance traveled by a point source situated just inside the waveguide. The important dimensions are illustrated in Fig. 4.9 below, and a summary of the design specifications is given in Table 4.3.

The phase variation across the face of the horn determines the quality of the incident radiation; ideally, the incident radiation would be a plane wave.

Table 4.3 - A summary of the H-plane horn specifications

Parameter	Value
b_1	12"
a	1"
ρ_1	18"
$\Delta\phi_{max}$	57.3°

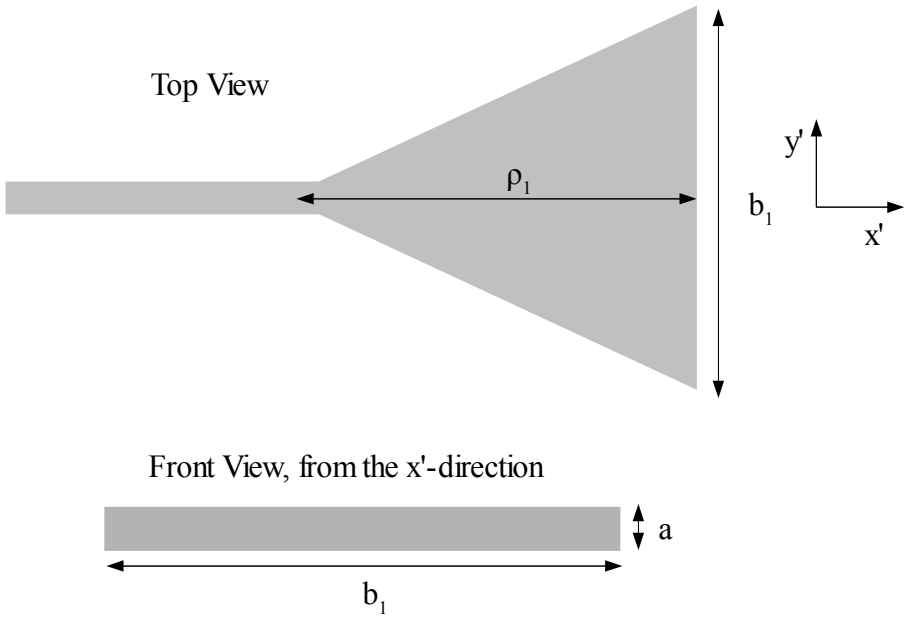

Figure 4.9 - The H-plane horn with waveguide feed

4.5.3 The Parallel Plate Section

The parallel plate section was designed so that it would contain only a TEM mode when operated at 6GHz. A TEM mode can always propagate in a parallel plate waveguide, but the higher modes are possible, with a cutoff wavelength given by [17]

$$\lambda_c = \frac{2d}{n} \quad (4.16)$$

where d is the plate spacing, and n is the index of the TE_{10} or TM_{10} mode. The n = 1 mode is the next mode up from the TEM mode, and thus, with d = 1", the cutoff wavelength is 2", corresponding to a frequency of about 6GHz. At 6GHz the TE_{10} mode is just starting to be present, but is very weak.

In order to maximize the gain, the plate spacing is chosen to be as large as possible without allowing higher modes (a bigger antenna means more gain). Thus d is chosen to correspond to the cutoff of the TE_{10} mode. A summary is given in Table 4.4.

Table 4.4 - A summary of the parallel plate specifications

Parameter	Value
Thickness, top	3/16"
Thickness, bottom	3/8"
Width	12"
Length	14"
d	1"
f_{c00}	0 GHz
f_{c10}	6 GHz

4.5.4 The Post Array Section

The post array section was designed to obtain a diffraction maximum at 60 degrees relative to the forward direction. This corresponds to a 30 degree Bragg reflection, as shown in Fig. 4.10. Bragg's Law of diffraction is given by Equation 4.1 where the m-th order beam at a given wavelength is scattered off a set of planes of posts a distance d apart, at an angle θ relative to the planes. A first-order Bragg reflection at 30 degrees relative to the plane of posts, with a plane spacing of 2", requires a wavelength of 2". If the equation is changed to the following:

$$\lambda = \frac{2\mathrm{d}}{m}\sin\theta \quad (4.17)$$

it can be seen that higher order reflections only occur for smaller wavelengths. In the

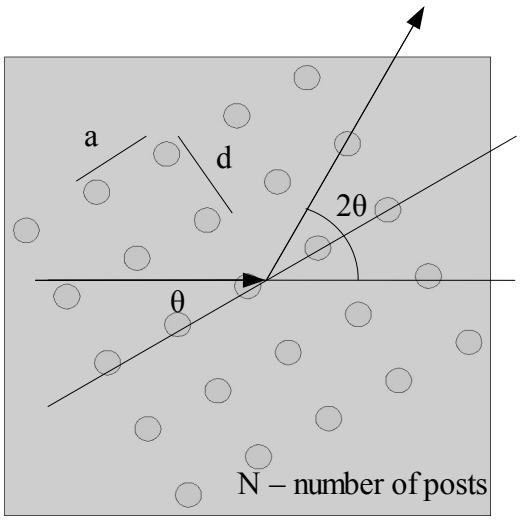

Figure 4.10 - Bragg diffraction

design at hand, a 6GHz feed is used, and so higher-order reflections can be neglected, since the next higher-order reflection would come at 12GHz. Longer wavelengths cannot "fit" in between the posts. It is thus seen that there is only one Bragg peak possible; the desired 6GHz peak.

From the Bragg Equation, it can be seen that three parameters must be fixed to get a maximum in a given direction: the wavelength, the plane spacing, and the angle of incidence. To change the direction of the beam, all three of these parameters must be readjusted. A summary of the important specifications for each section is given in Table 4.5 below.

Table 4.5 - A summary of the post array section specifications

Parameter	Value
d	2"
a	1"
θ	30°
λ	2"
Post diameter	¼"
N	56

4.6 Model Improvements Using GTD

The preliminary models used had a design similar to that shown in Fig. 4.7; the parallel plates were simply rectangular with flat edges, and the post array section was placed in between the parallel plates. In a simulation sweeping the angle of the post array, it was found that for certain angles the quality of the main beam was greatly reduced, with a large overlapping non-Bragg peak.

To resolve this issue, the Geometrical Theory of Diffraction (GTD) was used. In traditional optics, there is no mechanism to account for diffraction of a light wave passing by a sharp edge, or a point. If the ray misses the object, it simply travels past it, without effect. The GTD provides an explanation for such effects.

This theory classifies various fundamental geometrical shapes, and calculates the effect of such shapes on a grazing ray of light. Such shapes include edges, points, round objects, screens, and so on. For more complicated situations, a shape is broken down into

these constituent shapes, and the GTD calculates the effects for each shape; the total effect, then, is the superposition of the fields.

It should be clear from Fig. 4.7 that there are sharp edges on the parallel plates, as well as points on the corners. According to the GTD, the points diffract like point sources, while the edges have an associated diffraction cone. To eliminate the effects of the edges and corners, the parallel plates were altered to have a curved semicircular shape where the Bragg reflection leaves the parallel plates. Also, the edges were changed from flat to rounded. The justification for the smoothing of edges and elimination of corners is given in [13], where it was found that curvatures of a larger radius tend to have a less drastic effect on a nearby passing beam. The actual model change, and the results of the change, are given in chapter 5.

4.7 Switched Beam Antenna

Using the theory of X-ray crystallography, it is possible to design a switched beam antenna. In what follows, the theoretical principles will first be discussed. Next, a method in which the theory is applied to obtain a switched beam antenna will be given.

4.7.1 Reciprocal Space

Each crystal may be defined by its lattice – that is, its repeating motif. For example, a square lattice would consist of an infinite, regular, and repeating pattern of squares, an atom at each vertex. A rectangular lattice would have an infinite pattern of rectangles, with an atom at each vertex. The square has one parameter – its edge length;

and the rectangle has two parameters – the length of each of its two edges. Furthermore, each lattice has an associated reciprocal lattice. The reciprocal lattice is a mathematical construction that can be used to determine when X-ray diffraction will occur.

Using the mathematical prescription, the reciprocal lattice of a square lattice crystal is another square lattice; likewise for a rectangular lattice, it is another rectangular lattice. A square lattice with edge length "a" would have a square reciprocal lattice with length 1/a [18]. Thus for a crystal with an edge length of ½", the reciprocal lattice would be a pattern of squares with an edge length of 2 in^{-1}. The reciprocal lattice for such a case is shown in Fig. 4.11 below.

Similarly, for a rectangular lattice of edge lengths (a, b), the corresponding reciprocal lattice would be rectangular, or dimension (1/a, 1/b). In the case of a = ¼", and b = ½", the reciprocal lattice would thus be a repeating pattern of rectangles of edge length (2 in^{-1}, 4 in^{-1}), shown in Fig. 4.12 below.

Conceptually then, contracting the direct space square in one dimension to create a rectangle, going from a ½" spacing to a ¼" spacing, corresponds to expanding in the reciprocal space.

4.7.2 The Ewald Sphere

An elegant construction known as the "Ewald sphere" may be used in the reciprocal lattice to determine when a diffraction condition will exist. Given wavelength λ impinging on a crystal, a circle with radius $1/\lambda$ is constructed in reciprocal space.

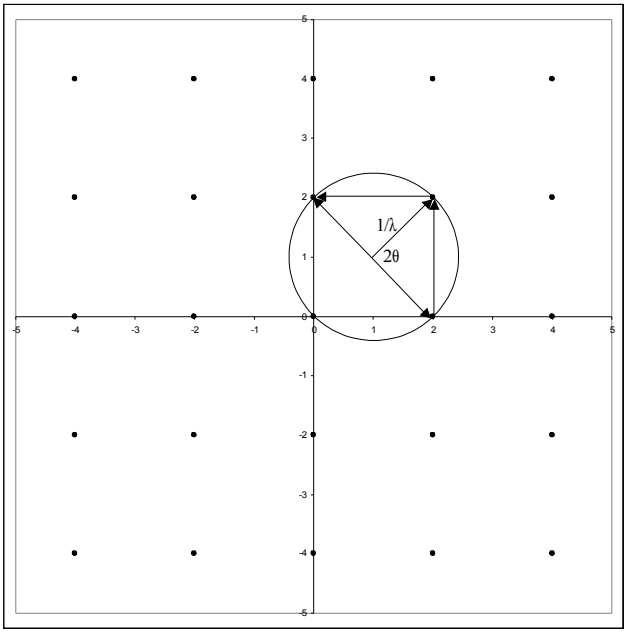

Figure 4.11 - Reciprocal lattice for a square crystal with edge length of ½"

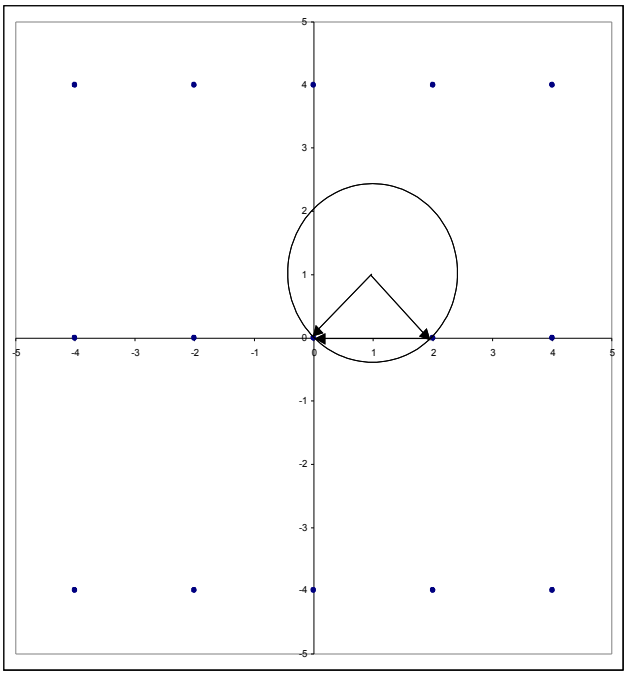

Figure 4.12 - Reciprocal lattice for a rectangular crystal with edge lengths of ¼", ½"

The circle may then be freely moved about in the reciprocal space, and if the circle intersects the reciprocal lattice at two or more points, a diffraction will occur. Referring to Fig. 4.11, if the wavelength is 0.707" then it is possible to get two 45 degree diffractions ($2\theta/2 = 90/2 = 45$ degrees relative to the Bragg plane), one for each vector with tip and tail on the circle. This would translate into diffractions at +/- 90 degrees relative to the incident beam. For the rectangular lattice of Fig. 4.12, the same wavelength will only yield one reflection, at 45 degrees. Thus, by shortening the spacing between atoms in one direction the diffracted beam goes from two directions to one.

4.7.3 A Switched Beam Antenna

To design a switched beam antenna, imagine a two dimensional square lattice of metal (or dielectric) posts in between a parallel plate waveguide. The radiation pattern would have two beams, going off at right angles to the incident beam. If, in the next instant, an additional metal post is inserted between each of the posts in one of the directions, (as in the case of Fig. 4.12), then there would be only one beam, traveling at 90 degrees relative to the incident beam. If this capability were possible in both directions, say both "a" and "b", then the beam could be switched between 90 degrees and -90 degrees.

To achieve this switching with metal posts, the posts would have to be mechanically removed from the parallel plate waveguide cavity, actuated electromechanically. If variable dielectric posts were used, the posts could be switched between $\varepsilon_r = 1$ (post off), and some value close to 5.

5. EXPERIMENTAL

As indicated in Chapter 3, there were two possible methods followed in this work. Either a claim was verified with HFSS simulation alone, or in the case of Bragg's Law it was verified both with HFSS simulation and experimental data. In this chapter, the computational requirements for the HFSS simulations, the HFSS models, and a description of the procedure for the verification of Bragg's Law are given.

5.1 HFSS simulations

The appendix shows the steps necessary for successfully simulating a model: A model is drawn, boundary conditions and excitations are assigned, the analysis setup is completed, and the results desired are extracted. A summary of these steps for each model used is presented herein, after a discussion of the system requirements for the simulations.

5.1.1 Computational System Requirements

The minimum system requirements for HFSS include 1GB of Random Access Memory (RAM), a processor that is 900 MHz or better, and a hard drive with enough space to hold all the data generated. Drastically more resources were needed for many of the simulations run here. The main limitation wasn't the processor speed or the hard drive space, but the RAM. As an illustration, the RAM requirements for the simulation exploring the effect of crystal size is shown in Fig. 5.1.

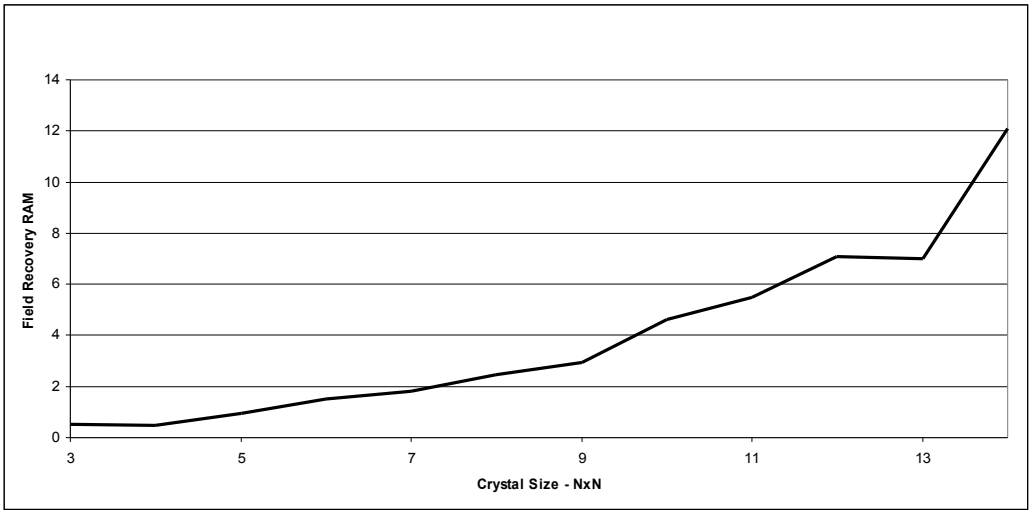

Figure 5.1 - The RAM requirements for simulations of the effects of crystal size

There are a few factors affecting the amount of RAM needed. The first, and perhaps most obvious, is the size of the model relative to the wavelength of the solution desired. For example, a 12"x14"x1" structure may be large for a 24 GHz (½ " wavelength) solution frequency, but it is small for a 1GHz (12" wavelength) solution. The useful metric is the ratio of the model volume to wavelength cubed. Of course, the solutions of interest are for smaller wavelengths, and thus require more RAM. The system used for the more intensive simulations was a 2.67GHz i5 quad core with 16GB of RAM.

5.1.2 Models Used

While numerous models were used, there are some basic boundary conditions that remain the same across all models. The first model considered will have a detailed picture of the model size, boundary conditions, excitations, and analysis setups. Subsequent models will be summarized more briefly.

5.1.2.1 Effect of Crystal Size

In verifying the effect of crystal size on the diffracted peak width, a scaled model was used for the various crystal sizes. The first model considered will be the case for a crystal of size 8x8 posts. The remaining sizes (from 3x3 to 14x14) are all scaled versions.

A top view of the 8x8 model is shown in Fig. 5.2. For all of the models in the exploration of the effect of crystal size on diffracted peak width, a 30 degree angle of incidence was used. The lattice was square, with the posts being spaced 1.25cm apart.

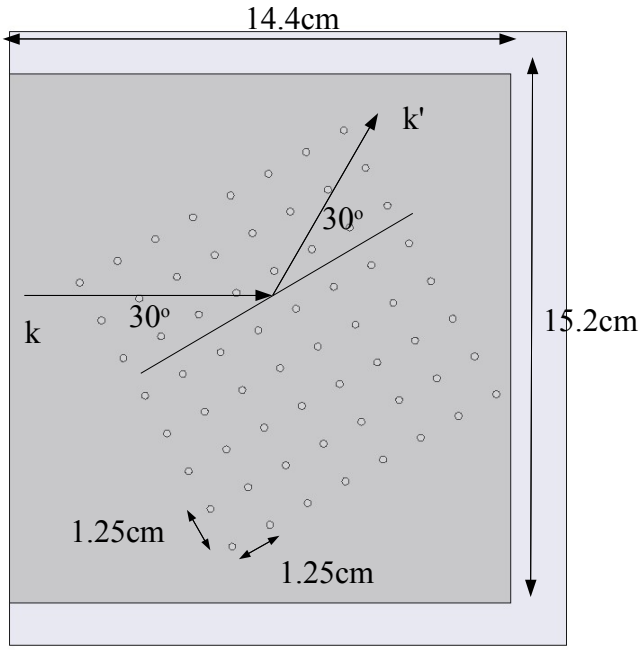

Figure 5.2 - A top view of the 8x8 model

The plates were placed 1cm apart, and the thickness of both the top and bottom plates was 0.1cm. The post radius was also 0.1cm. The plane wave was incident from the **k**

direction, as shown in the figure. The diffracted beam exited the structure in the **k'** direction.

A view from the [-1 -1 -1] direction is shown in Fig. 5.3. The direction of the incident beam is along the y direction; that is, the y direction and the k direction of Fig. 5.2 are parallel.

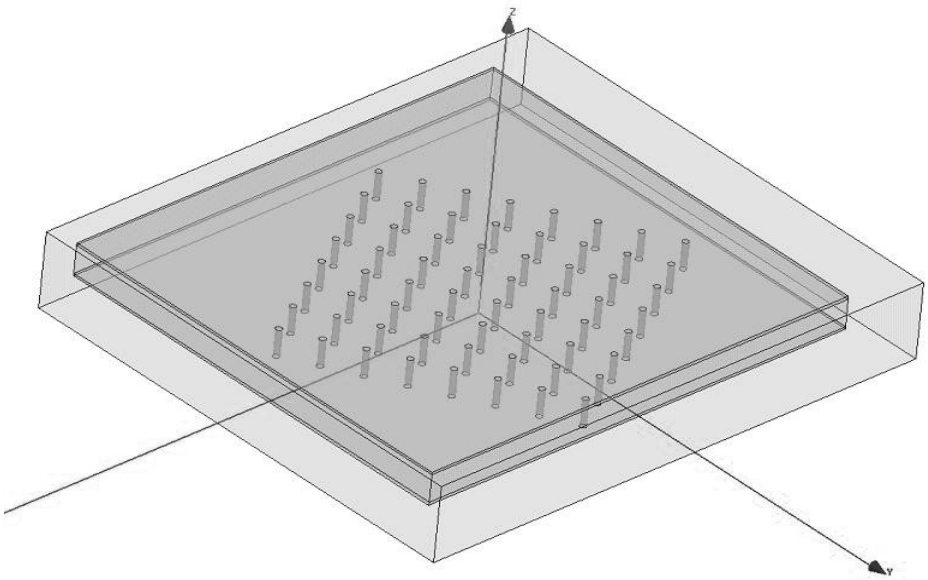

Figure 5.3 - A view of the 8x8 model from the [-1 -1 -1] direction

Having discussed the geometrical model, the next step in the process is to assign boundary conditions and excitations. The top and bottom plates, as well as the posts, all have Perfect Electrical Conductors (PEC) as a material assignment. The three sides along the opening of the parallel plates are assigned a Perfect H (perfH) boundary, so that the electric field can travel freely out of the structure. This is shown in Fig. 5.4. The wave port excitation enters at the back of the structure, as shown in Fig. 5.5. The wave

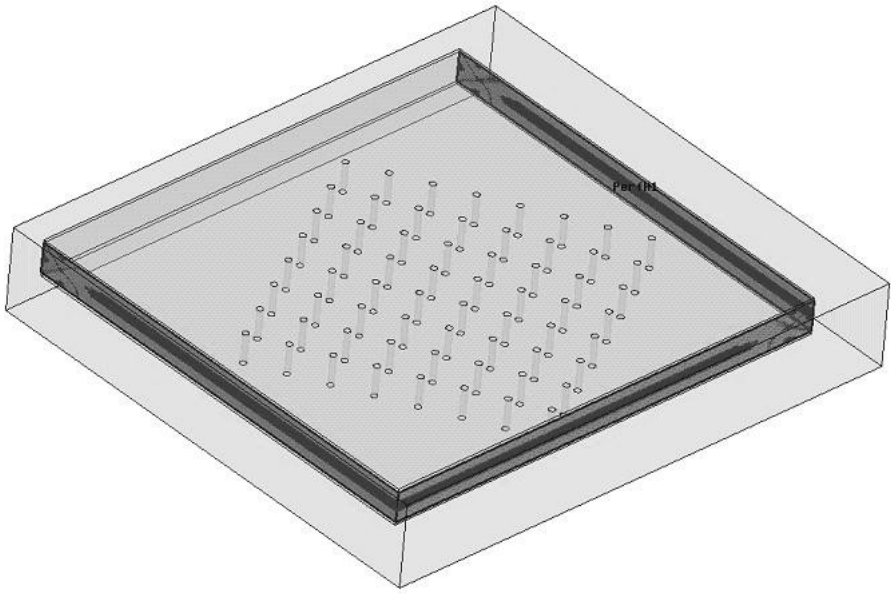

Figure 5.4 - The perfH boundary for the 8x8 crystal

port uses all of the default settings (e.g. no renormalization, and no polarization). Since this struc-ture is designed so that only the TEM mode propagates, the polarization does not need to be set (no integration line is necessary).

The only part of the model that hasn't yet been discussed is the large box enclosing the entire structure; because HFSS solves a structure inside of a volume, the model must be limited in size. However, if the far field radiation pattern is desired, it might seem that the model should be quite large. This would make the solution of all models needing a radiation pattern intractable. To deal with this problem in HFSS, therefore, the convention is to make a box enclosing the antenna. The box should enclose the antenna, but also be at least a quarter wavelength larger than the antenna in each dimension. HFSS can then calculate the far field pattern.

.

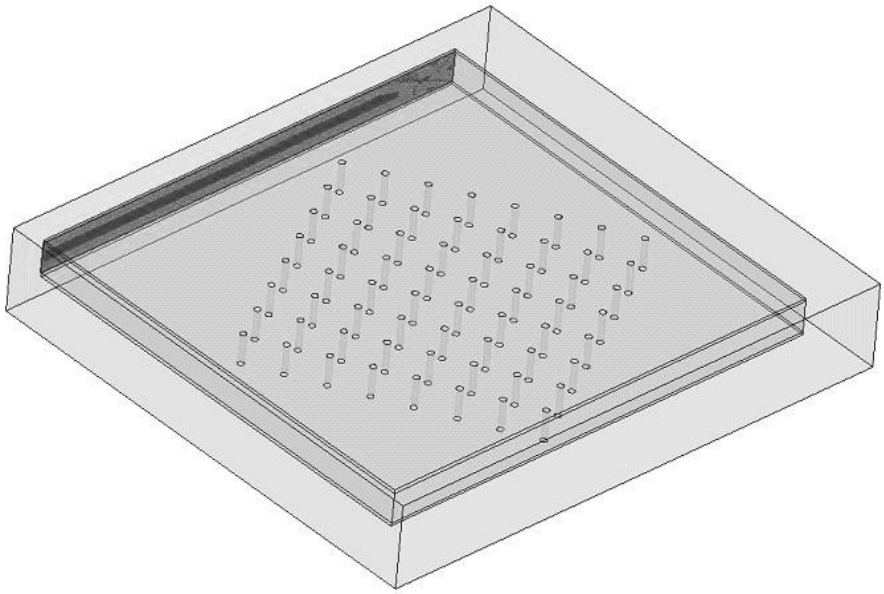

Figure 5.5 - The wave port for the 8x8 crystal

The size of the radiation box for this model is symmetrically placed about the parallel plate waveguide, except for the back wall, which shares a face with the wave port. The dimensions of the box for the 8x8 model are 11x10x2 ¾ cm. The radiation boundary is shown in Fig. 5.6.

The model geometry, boundaries and excitations have all been assigned for this model. The analysis setup is the next step in successfully simulating the structure. The solution desired was for 24 GHz, with the convergence criterion that the maximum change in s be 0.02 or less. The rest of the settings were all default. The dialog is shown in Fig. 5.7. A summary of the design characteristics for the 8x8 crystal is given in Table 5.1.

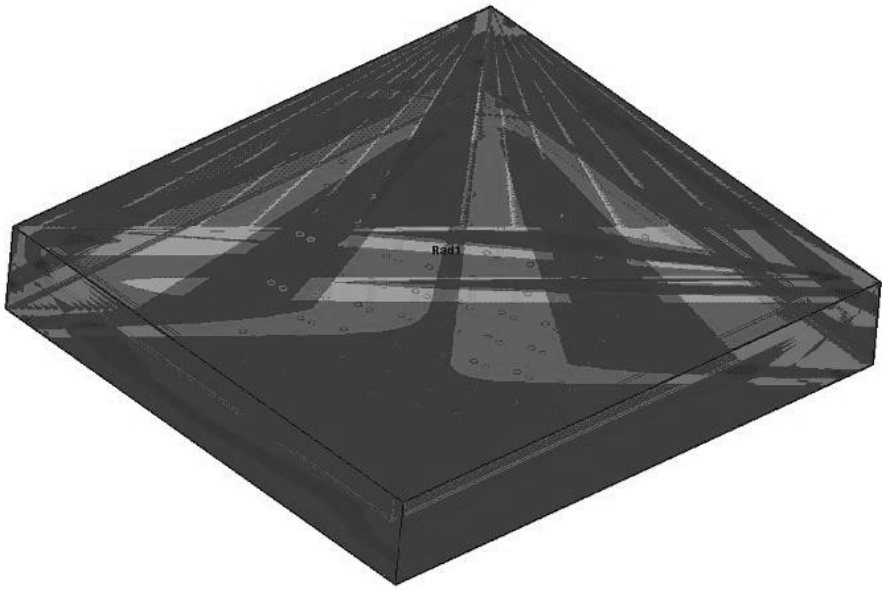

Figure 5.6 - The radiation boundary enclosing the 8x8 post array

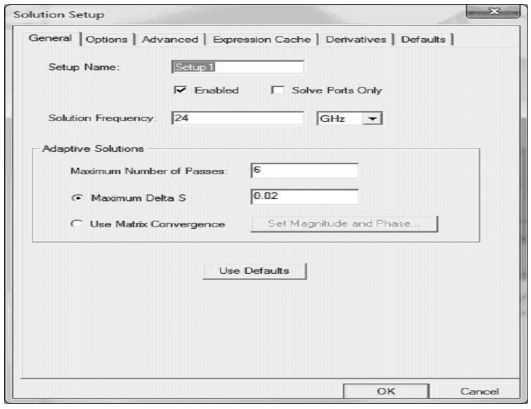

Figure 5.7 - The analysis setup for the 8x8 crystal

Table 5.1 - A model summary for the 8x8 crystal

Parameters	Value
Plate thickness - top	0.1cm
Plate thickness - bottom	0.1cm
Plate spacing	1cm
Crystal size	8x8
Post spacing	1.25cm
Post radius	0.1cm
Angle of incidence	30^{o}
Solution frequency	24GHz
Max. ΔS	0.02

This finishes the discussion of the 8x8 model. At this point, it is worthwhile to consider the scaling of the model when simulating larger or smaller structures. Scaled versions of the 5x5 model were used for crystal sizes ranging from 3x3 posts to 14x14 posts. As an example, the model for the 14x14 case is shown in Figs. 5.8 and 5.9. For the various designs, only the parallel plate waveguide and the radiation box were changed. The crystal was not scaled, but the number of posts was varied. Scaling was done only in the x- and y- directions, and not the z- direction. Resizing of the waveguide and radiation boundary were performed to accomplish the following:

1. Preserve the size of the parallel plate waveguide relative to the crystal, as the size of the crystal changes.
2. Preserve the placement of the crystal within the waveguide as the size of the crystal changes.

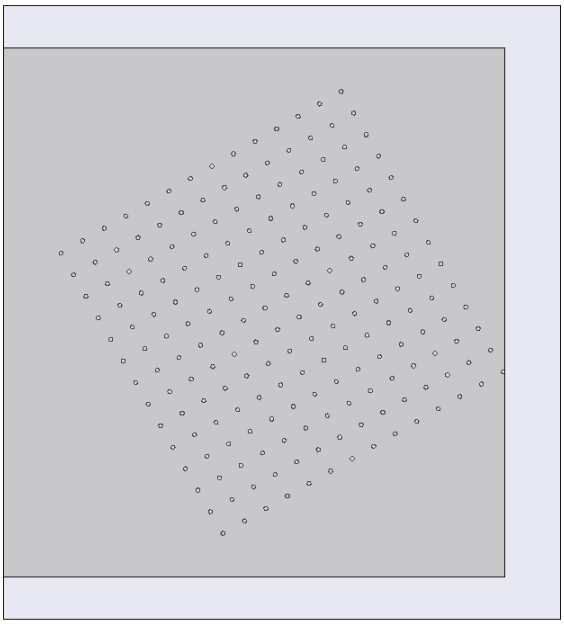

Figure 5.8 - A top view of the 14x14 model

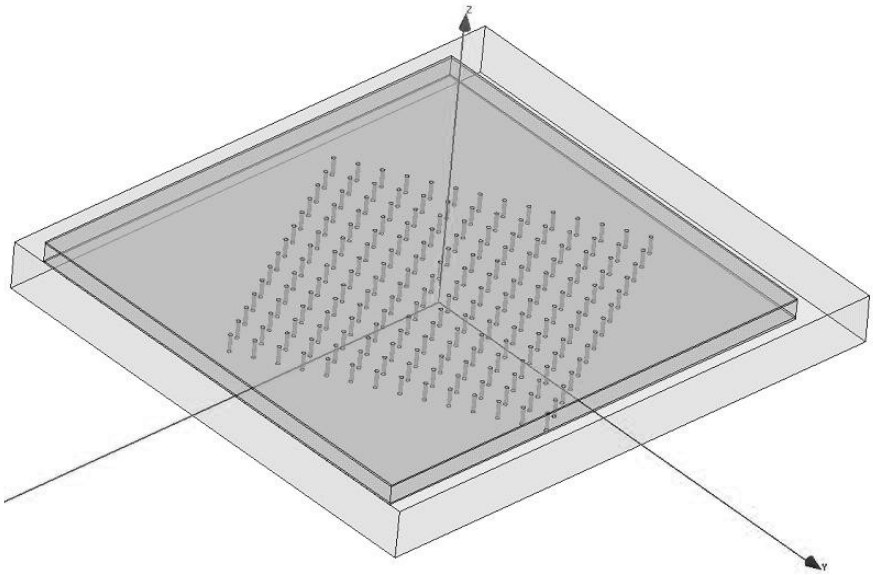

Figure 5.9 - A view of the 14x14 model, from the [-1 -1 -1] direction

This was accomplished fairly well by scaling in the x- and y- directions by a factor N/5, where N is the number of posts, and 5 is the number of posts used in the very first model. It was also necessary to shift the crystal within the waveguide to preserve its relative location within the waveguide. The crystal, in all cases, was centered at the origin.

5.1.2.2 A Model Improvement

For simulating the effect of crystal size, reasonable results were obtained with the model of the previous section. For the design exploring the effect of angle however, this model was insufficient. As the angle was varied, the scaling factors needed to be improved, and the corners and edges of the parallel plate waveguide began to degrade the quality of the data (see the discussion of the GTD, above). It was thus necessary to improve the model. The shape of the parallel plate waveguide was altered, and a new formula was used for scaling. The remainder of the simulations, apart from the verification of Bragg's Law at radio frequencies, used this model.

A top view of the improved model is shown in Fig. 5.10, and the view along [-1 -1 -1] is shown in Fig. 5.11. The boundary conditions are the same, as are the material assignments. The only difference is the model geometry and the analysis setup.

The geometry of the model changed in two ways: the straight edges of the parallel plate waveguide were rounded; and the front of the waveguide was changed into a semi-circle. This eliminated the edge effects on the straight portion, as well as the corner effects. A disadvantage of this model is that the curved section still has flat edges.

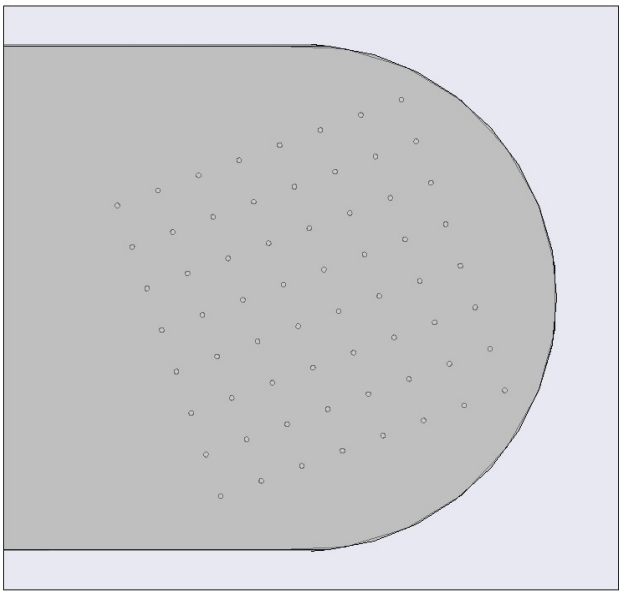

Figure 5.10 - A top view of the improved model

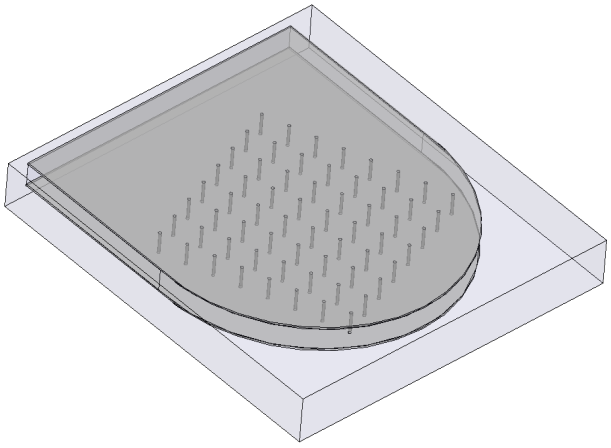

Figure 5.11 - Improved model, diagonal view

5.1.2.3 Bragg's Law and Various Other Simulations

The majority of the remaining simulations were carried out using the improved model. As the previous sections describe the detail of the models, this section consists of a summary of the following experiments: verification of Bragg's Law, effect of angle, post diameter, dielectric constant, and absorption.

To verify Bragg's Law, as well as the effect of angle on peak width, the same model was used. Table 5.2 summarizes the improved model information specific to this design. To set up the θ sweep, a parametric sweep was done; the values over which θ was varied are given in the table.

Table 5.2 - A summary of the parameters: Bragg's Law, effect of angle on beam width

Parameters	Value
Plate thickness - top	0.1cm
Plate thickness - bottom	0.1cm
Plate spacing	1.25cm
Crystal size	8x8
Post spacing	$\lambda/(2 \sin\theta)$
Post radius	0.1cm
Angle of incidence	22^{o}-46^{o}, 2^{o} steps; 45^{o}
Solution frequency	24GHz
Max. ΔS	0.01

For scaling in the x- and y- directions, a more thorough formula was used. Also, a formula for the centering of the crystal with the origin was used. The following three constraints were used to scale:

1. Post spacing was scaled with wavelength, according to Bragg's Law.
2. The corner of the crystal closest to the edge of the waveguide was kept, proportionally, at the same distance from the edge.
3. The relative cross-sectional areas of the crystal, parallel plate waveguide, and radiation box remained constant.

In Fig. 5.12 is a summary of the design variables. The position of the post closest to the edge of the waveguide is represented by "xf", the swept angle is "_theta", and the constant relative area is "Const." The formula for xf was found using the rotation transformation, and the formula for scaling y was found with the area constraint. Note

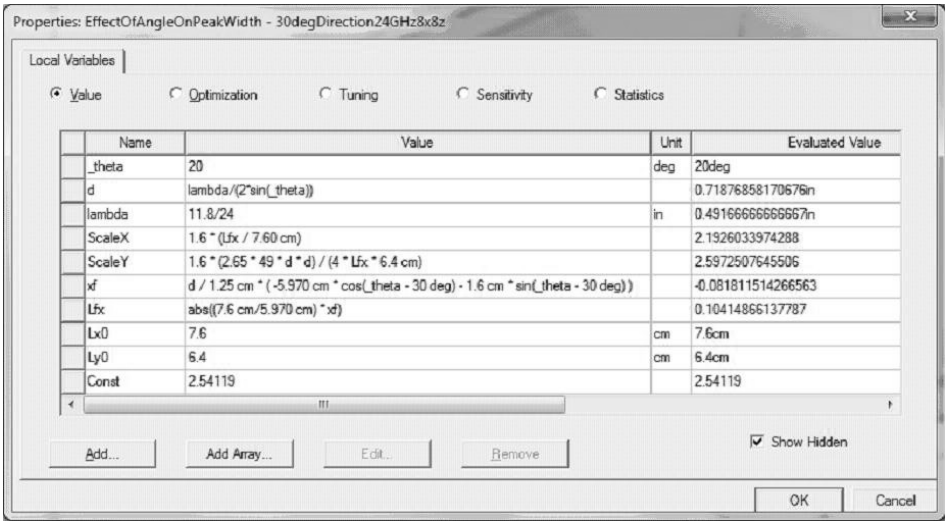

Figure 5.12 - The scaling formulas: Bragg's Law, effect of angle

that in the formula for xf, the rotation formula is shifted by 30^{O}. This is because the reference model is 30^{o}.

To simulate the effect of a change in post diameter, the same model was used. This model was simpler, as it did not require scaling. A summary of the parameters is given in Table 5.3.

The effect of changing the dielectric constant was also simulated; this case is much the same as for the change in post diameter, other than that a different variable was swept. A summary of the parameters is given in Table 5.4. Absorption is also similar, with a summary of its parameters in Table 5.5.

Table 5.3 - A summary of parameters for determining the effect of post diameter

Parameters	Value
Plate thickness - top	0.1cm
Plate thickness - bottom	0.1cm
Plate spacing	1.25cm
Crystal size	8x8
Post spacing	1.25cm
Post radius	0.025-0.2cm, 0.025 step.
Angle of incidence	30^{o}
Solution frequency	24GHz
Max. ΔS	0.01

Table 5.4 - A summary of parameters for determining the effect of post dielectric

Parameters	Value
Plate thickness - top	0.1cm
Plate thickness - bottom	0.1cm
Plate spacing	1.25cm
Crystal size	8x8
Post spacing	$\lambda/(2 \sin\theta)$
Post radius	0.1cm
Angle of incidence	30^{o}
Solution frequency	24GHz
Max. ΔS	0.01
Relative permittivity, ε_r	1-3.4, 0.2 step.

Table 5.5 - A summary of the parameters in the experiment on absorption

Parameters	Value
Plate thickness - top	0.1cm
Plate thickness - tottom	0.1cm
Plate spacing	1.25cm
Crystal size	8x8
Post spacing	1.25cm
Post radius	0.1cm
Angle of incidence	0^{o}
Solution frequency	24GHz
Max. ΔS	0.01

5.1.2.4 Physical Verification

The designs simulated above provided for a means of establishing Bragg's Law at RF via software. However, an antenna was designed, built, and tested for the same purpose. As a means of comparison, an HFSS model was created for this antenna. The dimensions and specifications of the model are the same as given in Section 4.5 above, Tables 4.2 - 4.5. The HFSS model is shown in Figs. 5.13 and 5.14 , below.

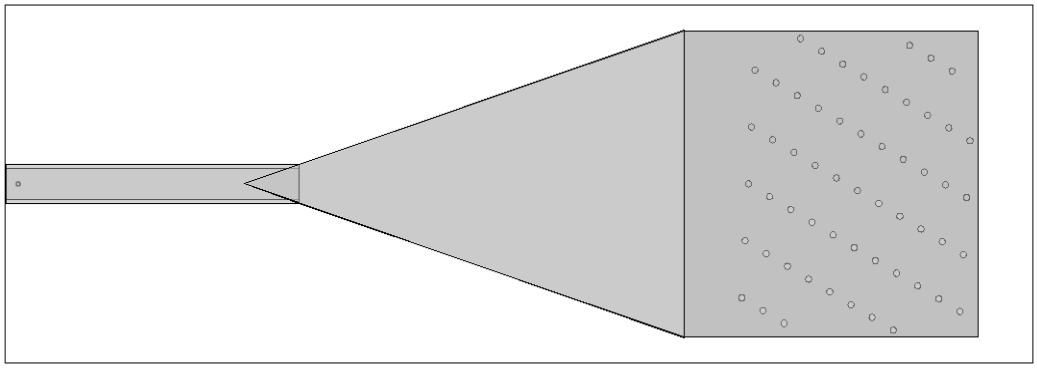

Figure 5.13 - Prototype Antenna - HFSS Model, Top View

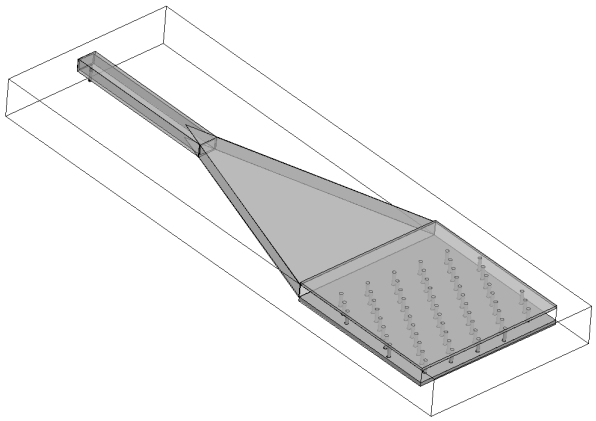

Figure 5.14 - Prototype Antenna - HFSS Model, Diagonal View

5.2 Verification of Bragg's Law at Radio Frequencies

As mentioned in Section 5.1.2.4, a prototype antenna was designed to verify Bragg's Law at RF. Here the construction and experimental setup used to characterize the prototype is explained.

5.2.1 Prototype Construction

The parallel plate section of the antenna was created using a mill to drill holes in the aluminum. The plates of aluminum were rotated 30 degrees and secured onto the drilling surface of the mill. The mill had an accurate digital readout, which was used to drill rows of 1-inch spaced holes, the rows being 2 inches apart. Because the aluminum plates were rotated 30 degrees, the rows of holes were at an angle to the edges of the plate. The holes were drilled just big enough for ¼ inch diameter bolts through.

To space the parallel plates, 1-inch lengths of 7/8-inch diameter PVC pipe were placed between the plates, visible in Fig. 5.15. Pipes were placed at each of the four corners of the post array section plus one more near the middle. The bolts were then put through the holes, forming the post array and fastening the parallel plates together.

The horn section was cut from aluminum sheet metal, and screws were placed to attach the horn section to the parallel plate section. The screws had small heads, so as to protrude as little as possible into the parallel plate waveguide. The horn then attached to

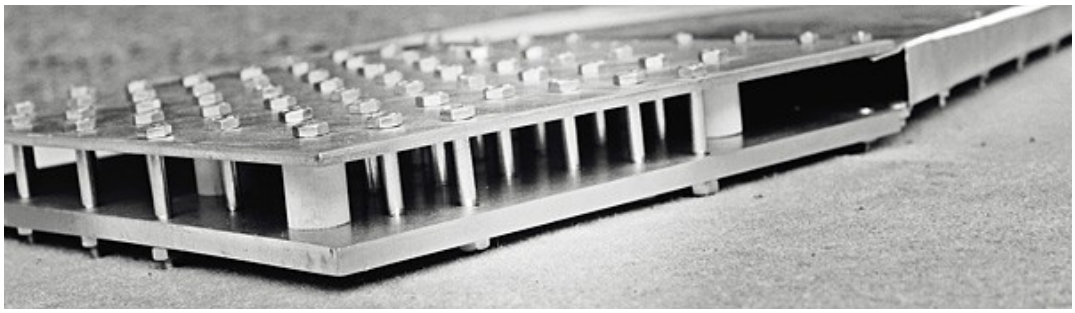

Figure 5.15 - Prototype antenna, view of post array section

a hollowed rectangular aluminum bar via screws, and the end of the bar had a shorting plate screwed onto it. A hole was drilled in the center of the E-plane, ½ inch from the shorting plate, with a diameter suitable for an N-type female connector with four mounting holes. The panel mount stub was then attached to the rectangular tube via four screw holes. Tuning of the waveguide to coaxial adapter section was attempted, but the best performance was obtained with no tuning screw installed. Refer to Fig. 5.16 below.

5.2.2 Measurement Setup

The antenna measurements were performed in a CATR, courtesy of Space Systems Loral. The antenna was placed on a homemade rotating table with degree marks to measure the angle. An Agilent 8720ES network analyzer was calibrated for two port use, port one being connected to the antenna with a 14 ft. cable, and port two connected via a 30 ft. cable to a waveguide to coax adapter, used as a receiving antenna. The test cables used were SMA, so an N-type to SMA adapter was used between the prototype antenna and the test cable attaching to the network analyzer. The antenna was swept from 5.85GHz to 6.65GHz with 801 points at selected angles from 0 to 180 degrees.

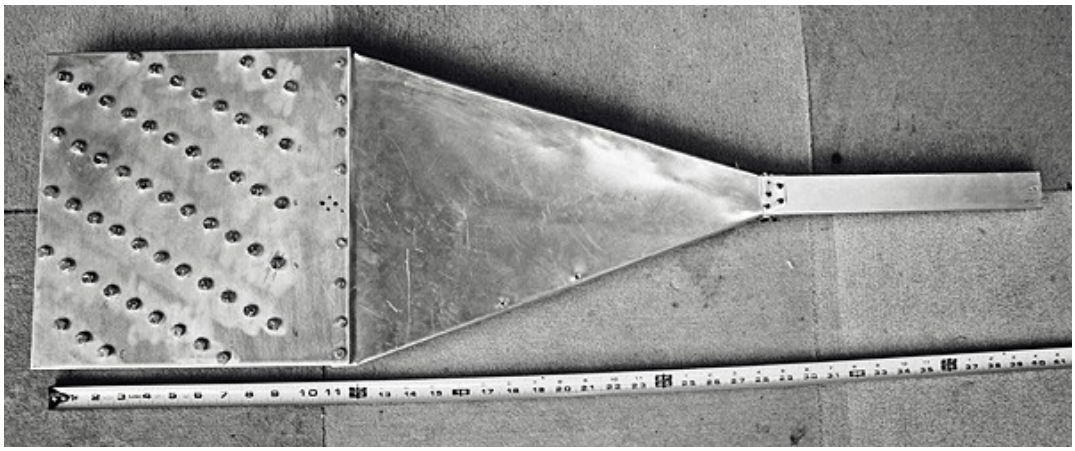

Figure 5.16 - Top view of prototype antenna

The receiving antenna was placed on a tripod, 15 ft. away from the prototype antenna. This distance was chosen so that the far field requirement would be met, at $2D^2/\lambda$, where D is the largest dimension of the antenna and λ is the wavelength. The edge length of the antenna aperture was 12 inches and the wavelength at 6GHz is 2 inches, for a far field requirement of 12 feet. Refer to Fig. 5.17 for a diagram of the experimental setup.

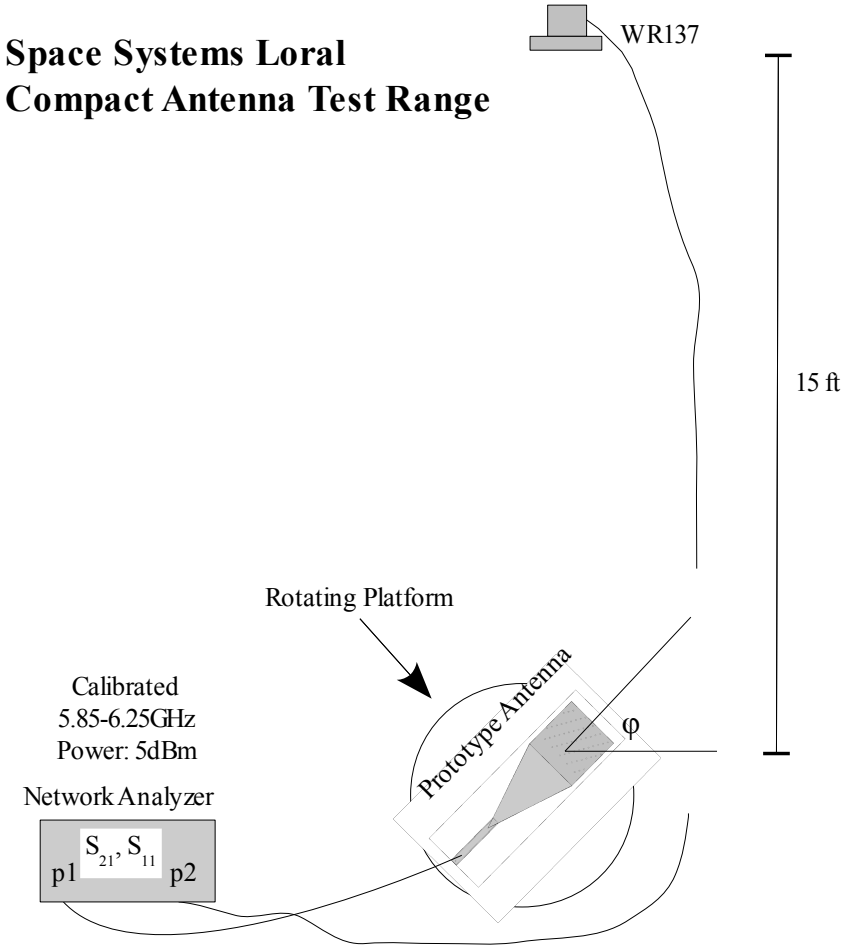

Figure 5.17 - Experimental setup at Space Systems Loral CATR

5.2.3 Switched Beam Antenna

In Section 4.7 the Ewald circle was introduced as a tool to determine when a diffraction would occur, and a prescription for a switched beam antenna was given. In this section, the HFSS model for a switched beam antenna will be presented.

Consider the model of Fig. 5.18a; each post consists of a material that can switch between a dielectric constant ε_r=1 or 2.4. The array pictured below can be thought of as three arrays, interwoven together. Each lattice can be turned "off" (ε_r=1) or "on" (ε_r=2.4). The main array can be thought of as the "primary" array, shown in Fig. 5.18b. With only this array on, diffracted beams are created at right angles to the long edges on either side.

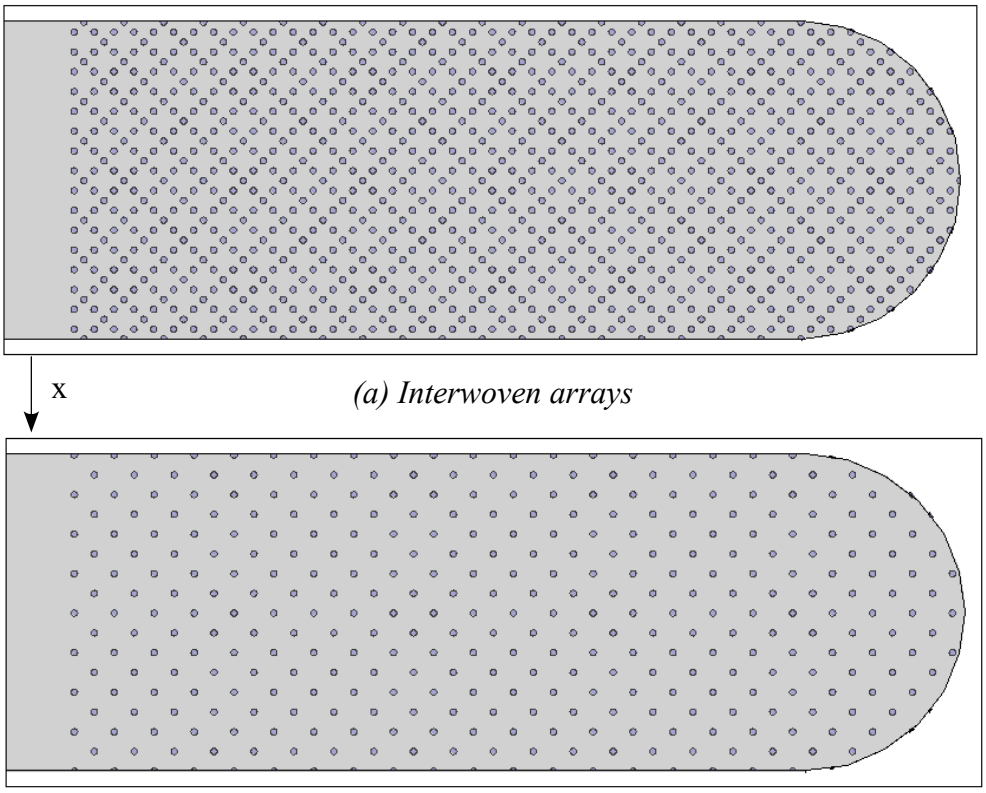

(a) Interwoven arrays

(b) Primary array

Figure 5.18 - Switched beam antenna

The "secondary" arrays are paired with the primary lattice to form a beam at a right angle to one long edge of the antenna or the other; each of these possibilities are shown in Fig. 5.19. In other words, when one of the secondary arrays pairs (i.e., one primary and one secondary array are "on") with the primary array of Fig. 5.18b it forms the array of Fig. 5.19a; when the other secondary array pairs with the primary array, the array of Fig. 5.19b is formed.

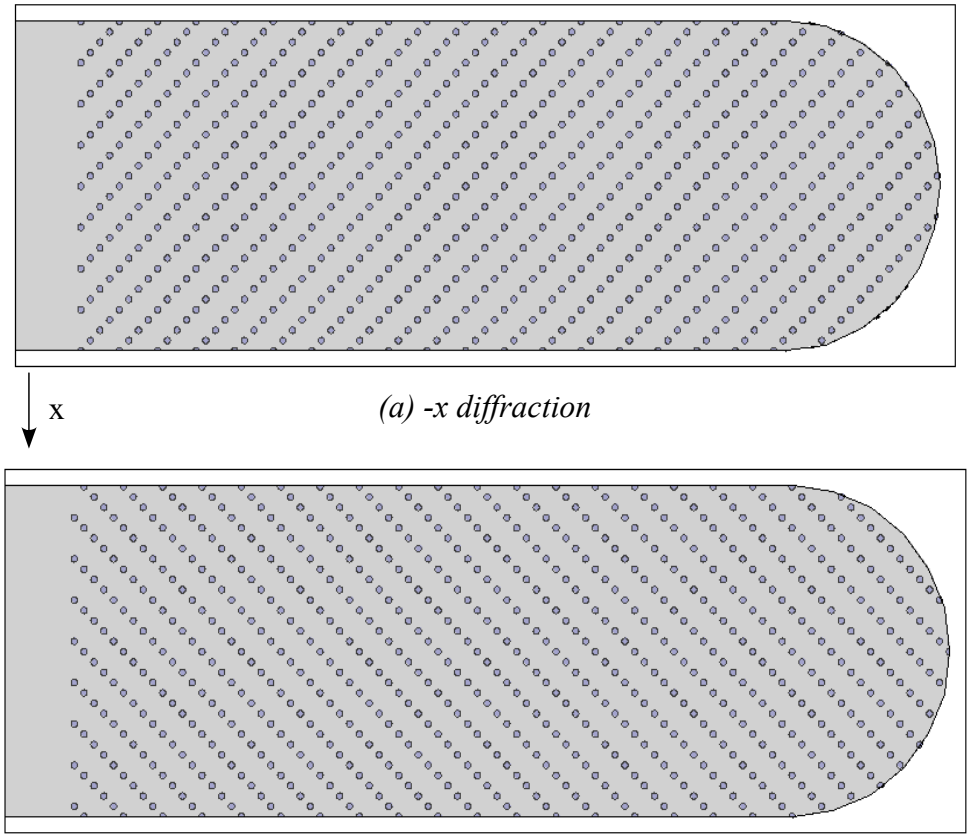

(a) -x diffraction

(b) +x diffraction

Figure 5.19 - Altered switched beam antenna

The view of Fig. 5.20 shows the curved frontal opening of the parallel plate waveguide. In this model, a perfect-E boundary condition was set along this curved face of the antenna to act as a beam stop, so that the undiffracted beam would be blocked. A summary of the model dimensions is given in Table 5.6.

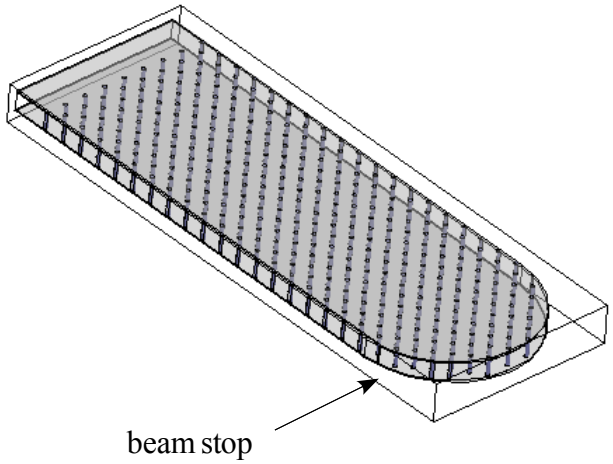

Figure 5.20 - Switched beam antenna beam stop

Table 5.6 - Switched beam antenna model parameters

Parameter	Value
Parallel plate spacing	1.0cm
Plate thickness	0.1cm
Parallel plate width	10cm
Parallel plate length	25cm
Post spacing	0.8831 cm
Post radius	0.1cm
Angle of incidence	45^{o}
Solution frequency	24GHz
Max. ΔS	0.02

6. RESULTS AND DISCUSSION

In Chapter 5, the setup of various experiments was described. The results of the experiments will now be presented, along with a discussion of the results.

6.1 Crystallographic Quantities

The first results to be considered will be those crystallographic laws verified with simulation only, and not an actual, experimentally tested model. Refer to the flow chart of Fig. 3.1.

6.1.1 Effect of Crystal Size

In Section 4.3.2 above, the effects of crystal size on beam width were predicted to follow the Scherrer equation (4.3). The Scherrer equation may be rewritten

$$B = \frac{K\lambda}{N d \cos\theta} \quad (6.1)$$

In this experiment the wavelength, λ; the angle of incidence, θ; and the plane spacing, d; are all fixed. The parameter varied is the crystal size N. By varying the crystal size, a set of Bragg peaks is obtained, and the peak width B is extracted. The shape factor, K, can then be found by fitting the data to this curve.

The results of the experiment of Section 5.1.2.1 are given in Fig. 6.1 below. The value of the shape factor K that gave the best fit between the curves was 1.024 and the residual error squared was 0.013. As is apparent from the graph, the general dependence of the peak width on the crystal size is captured well: the peak width decreases as crystal

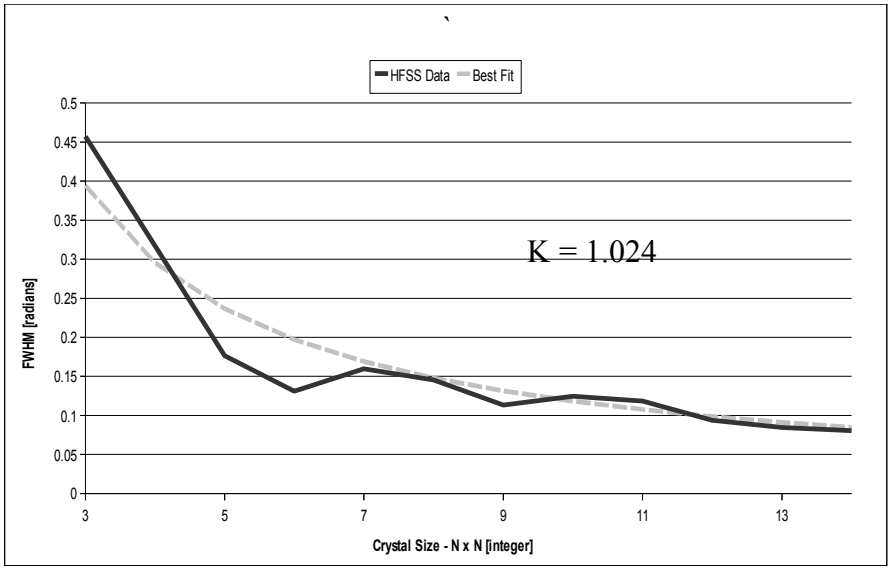

Figure 6.1 - The effect of crystal size on peak width

size increases. However, the best fit is rather poor at lower crystal sizes. This may be due to the fact that as the crystal size becomes smaller, the set of posts becomes less like a crystal – the limiting case, of course, being one post by itself.

The quality of the result may also be affected by the convergence criterion, and the quality of the model. Tighter convergence (i.e., a smaller value for the max. Δs) could be used; or the improved model might be used for finding the effect of crystal size, as this excludes the effect of non-Bragg diffractions.

6.1.2 Effect of Angle

In Section 4.3.2.2 above, the effect of angle on the beam width was predicted to follow a modified version of the Scherrer equation,

$$B = \frac{2K}{N} \tan\theta \quad (6.2).$$

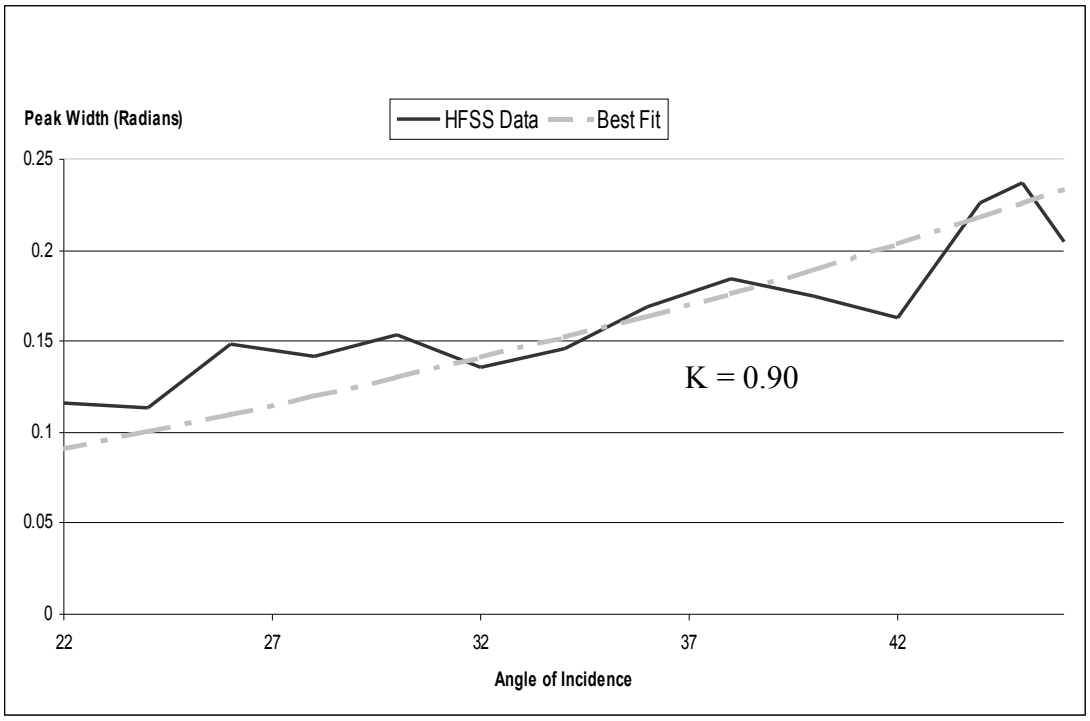

Figure 6.2 - The effect of angle on peak width

The results of the experiment described in Section 5.1.2.3 are given in Fig. 6.2. The value of the shape factor K that gave the best fit was 0.904, and the residual error squared was 0.006. Once again, the general dependence of the graph is qualitatively correct: as angle increases, so does beam width. Stated another way, the angular resolution decreases as the scan angle increases. The fit this time is a bit better than the fit in Fig. 6.1. Note also that the shape factors, which should be the same in both experiments (since both crystals are square), are different. These discrepancies are probably due to the fact that a reasonably large crystal (8x8) was used for each angle. The improved model model was also a contributing factor. The accepted value for K [19] is 0.93. The results above show good agreement with this figure.

6.1.3 Bragg's Law

While measuring the effect of angle on beam width, the angular location of the Bragg peaks was also extracted. The results of the simulation, along with the predicted values for the Bragg peak and the deviation from the prediction, are given in Table 6.1.

Table 6.1 - Verification of Bragg's Law

Bragg's Law	HFSS Model	
90+2θ	90+2θ	Δ
134	134	0.0%
138	138.5	0.4%
142	141.5	0.4%
146	145.5	0.3%
150	150	0.0%
154	154.5	0.3%
158	159	0.6%
162	164.5	1.5%
166	168	1.2%
170	172	1.2%
174	178.5	2.6%
178	179	0.6%
180	182	1.1%
182	183.5	0.8%
	Average	0.80%

In observing this data, it is evident that using Bragg's Law to predict the location of the maxima is extremely accurate, with the average error being only 0.8%. This confirms the validity of Bragg's Law at radio frequency. The setup for this simulation is given in Section 5.1.2.3 , Table 5.2.

6.1.4 Effect of Post Diameter

In Section 4.3.4.1, it was seen that the effect of increasing the post diameter was to increase the scattering power of each post. The relevant quantity is the structure factor, given by Equation 4.11.

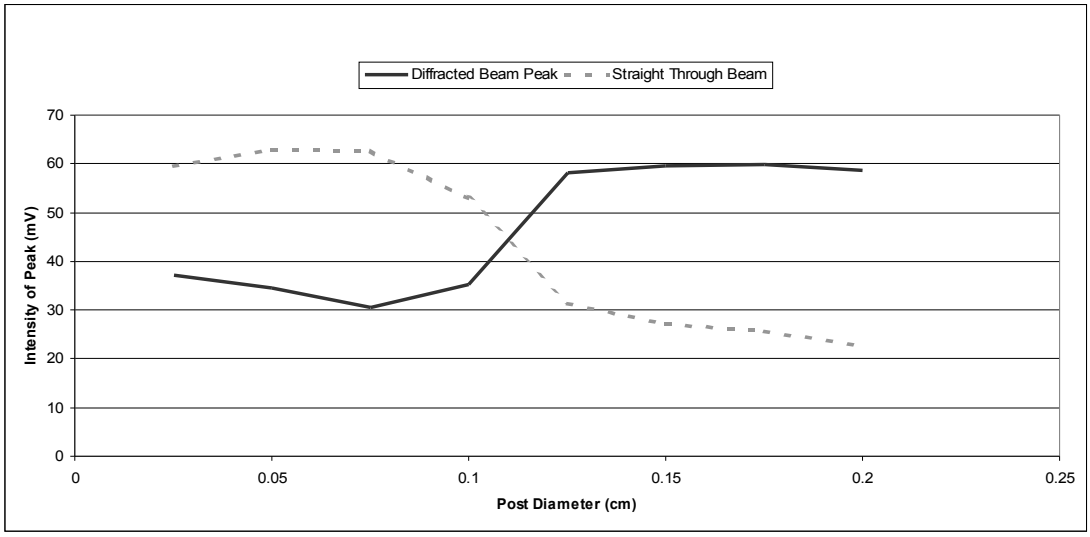

Figure 6.3 - The effect of post size on the diffracted and undiffracted beams

The results of the experiment described in Section 5.1.2.3 are given in Fig. 6.3. The results are intuitively obvious: smaller posts have less scattering power, and therefore more of the beam escapes through the undiffracted (dashed line), straight-on direction. Thus at smaller post diameters, the undiffracted beam magnitude is larger. As the post diameter increases, less of the beam passes through, and more of it is diffracted (solid line); hence the diffracted beam becomes more intense at higher post diameters. At about 0.1 cm, changes in post diameter have a more significant effect on the diffracted beam intensity. Above 0.125 cm, increasing post diameter has almost no effect.

6.1.5 Effect of Dielectric

Another possible way of changing the scattering power of posts is varying the strength of the dielectric constant, as found in Section 4.3.4.2. Again, the relative quantity is the structure factor.

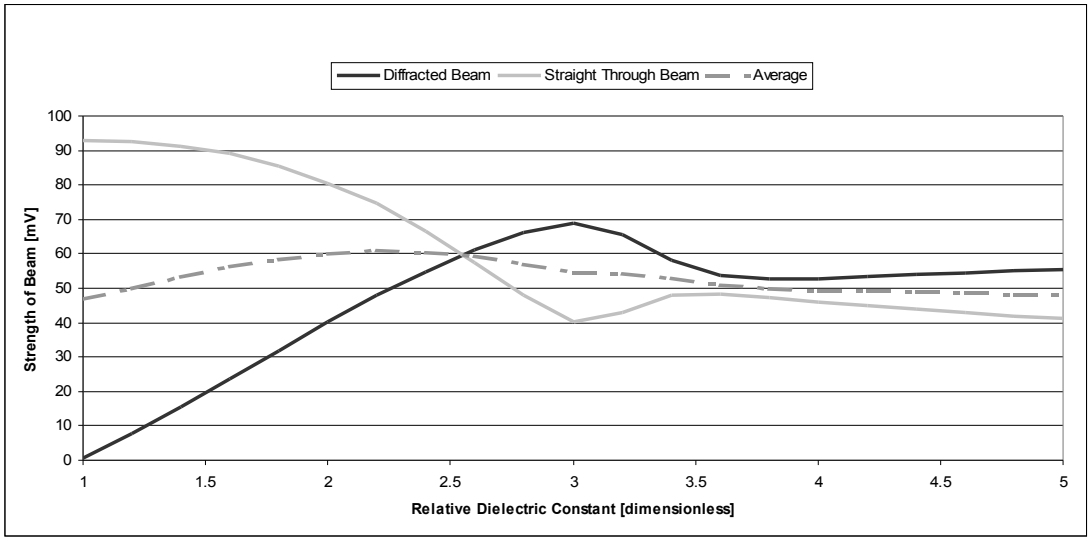

Figure 6.4 - The effect of relative dielectric strength

The results of the experiment described in Section 6.1.5 are given in Fig. 6.4. Up until a dielectric strength of about three, the results make sense: at a value of unity, the dielectric strength is the same as air; thus none of the beam is diffracted. Increasing from unity, more of the beam is diffracted. This is consistent with the scattering power of the beam increasing as ε_r increases. What appears to be an anomaly occurs after $\varepsilon_r = 3$: the scattering power starts decreasing again. From the nature of the variations in maximum beam height, it appears that as one beam gets stronger, the other gets weaker, and roughly in proportion. However, after about $\varepsilon_r = 2.5$, the average of the two beams (dashed) starts

to decrease. This suggests that there are other directions, other than diffracted and straight through, that begin to "steal" energy (which is also apparent from visual inspection of the graphs). With an array having an ε_r of unity (nearly equivalent to air), it is expected that a regular parallel plate radiating into space would be obtained; this was observed to be the case. At some value of ε_r, the antenna will be acting most like an array of posts exhibiting Bragg diffraction. It would appear that this value is at roughly 2.25, since this is when the average of the beams is a maximum. A maximum would indicate that there are the least number of other directions into which energy is escaping.

In the terminology of Section 4.3.4.2 it is clear that the optimal design would be attained at 2.25. Unfortunately, this value of dielectric does not give a diffracted beam that is stronger than the undiffracted beam. This model might be improved by increasing the number of posts.

6.1.6 Absorption

The absorption of the RF beam by the crystal was described in Section 4.3.3, and a summary of the experimental setup given in Table 5.5. Recall that this model is the same as that used for quantities explored, such as the effect of dielectric variation, above. The results are given in Fig. 6.5 below. The main features of the radiation pattern for this model were the main beam, which went straight through, and beams scattered off to the sides, at right angles on either side of the incident beam. The figure gives a plot of the maximum beam for different numbers of rows and the magnitude of the scattered side beam. The straight-through data is fit to an exponential function. Other fits were tried,

but the other fit that was closest was linear. For the exponential, an R-squared value of 0.9717 was obtained, and for the line a value of 0.9695. The exponential appears to have been the best match. A summary of the results is given in Table 6.2.

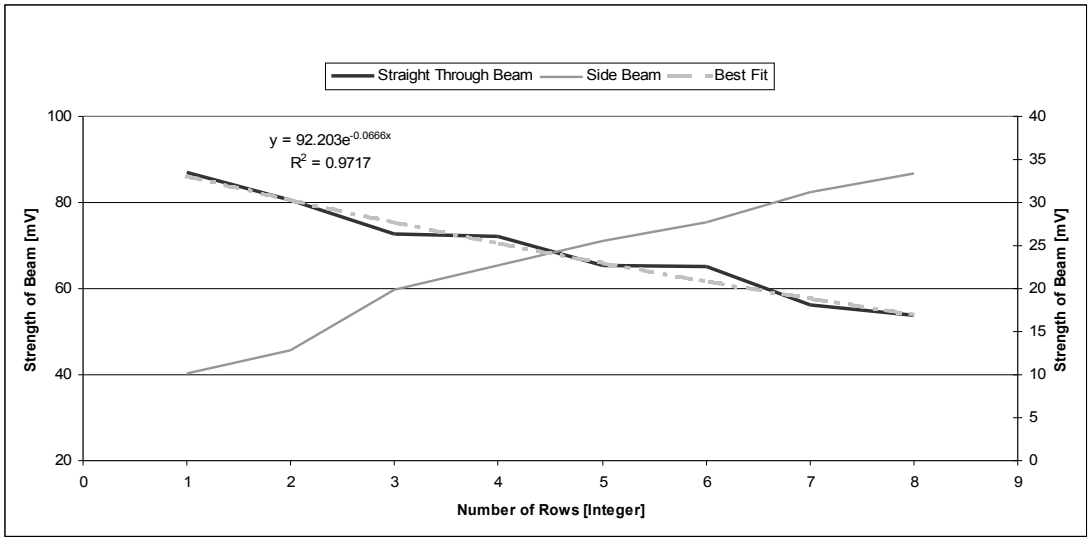

Figure 6.5 - Absorption of a lattice of the incident beam by the post array section

Table 6.2 - The results of the simulation on absorption

Quantity	Value
μ	0.0666
I_o	92.2000
R^2 – exponential	0.9717
R^2 – linear	0.9695

6.2 Verification of Bragg's Law

In Section 5.2 the experimental setup for the measurement of the prototype antenna was described. Here, the results of the experiment are given, comparing the HFSS simulations and experimental data. Next are the performance results.

6.2.1 HFSS Simulation vs. Experimental Data

As stated in Section 5.2.2, the prototype antenna was frequency swept from 5.85GHz to 6.65GHz, rotated through angles varying from 0 to 180 degrees. In this way, 801 radiation patterns were obtained, one for each frequency. The various radiation patterns were normalized and compared to the HFSS simulation for all frequencies.

As a measure of the quality of agreement, the deviation of each measured radiation pattern from its corresponding HFSS simulated radiation pattern was calculated, and absolute values summed. Radiation patterns corresponding to the mininum, maximum, and average deviation are given in Figs. 6.6 through 6.8.

The first plot, Fig. 6.6, shows the best overall agreement and minimum deviation from simulation. The measured diffracted beam (in black) barely deviates from the HFSS model (in gray). The undiffracted beam and other peaks are reasonably close to the HFSS predictions. Fig. 6.7 gives a top view of the predicted radiation pattern obtained for the best overall agreement, superimposed on the prototype antenna.

The plot of Fig. 6.8 gives an average or typical deviation from the model. Note that even though the agreement is not as close, the diffracted peaks still match up closely. This is typical of the majority of the plots. Even though the simulation and measured data do not match up closely over much of the plot, the location of the diffracted peak matches and is the strongest peak. Also, the undiffracted peak is typically the next strongest and is located at around 100 degrees.

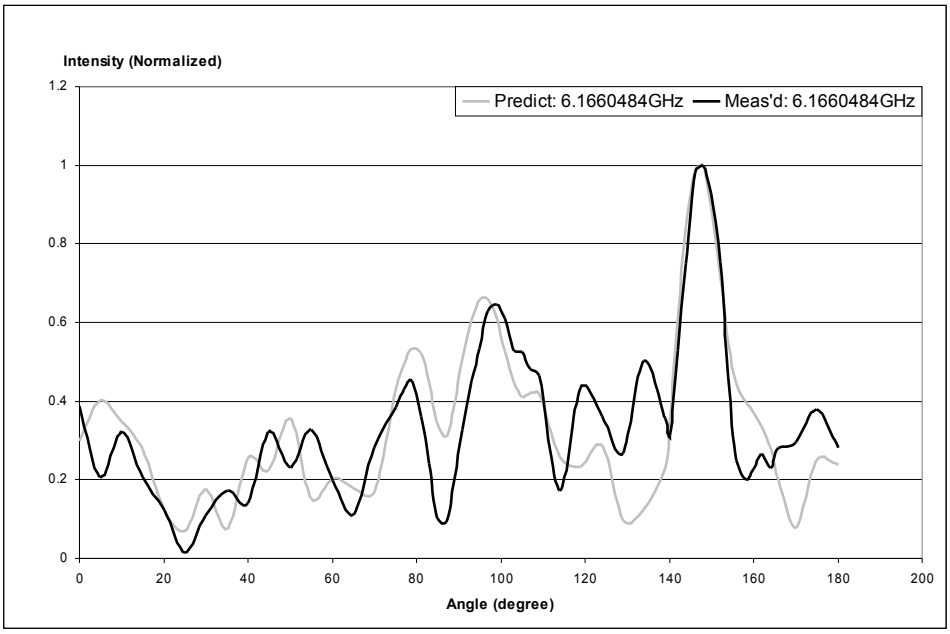

Figure 6.6 - S21, Best agreement between HFSS model and measurement

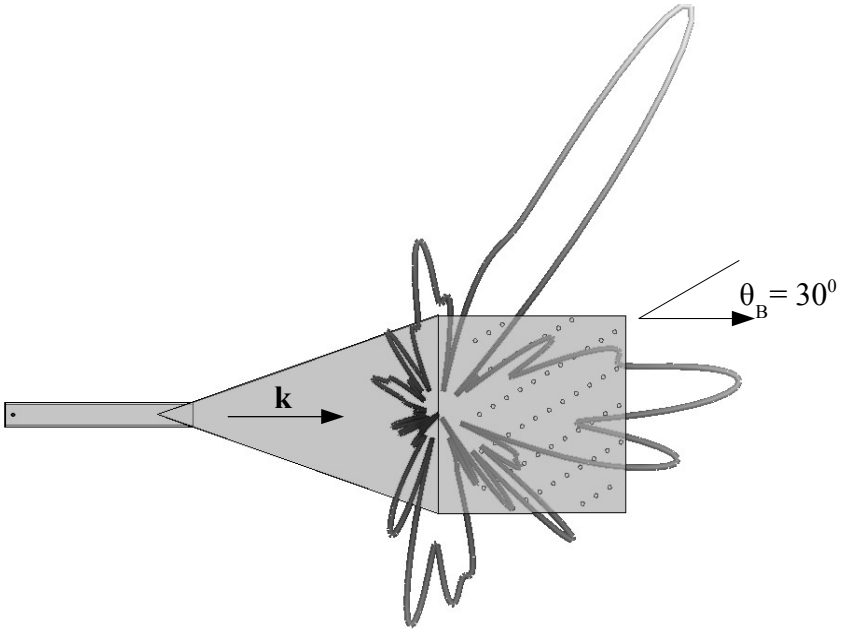

Figure 6.7 - The predicted radiation pattern, best case agreement

Even for the case of worst deviation the experimental radiation patterns still show the diffracted beam as the most prominent. Even at the worst matching frequencies, the diffracted beam still matches with the simulation.

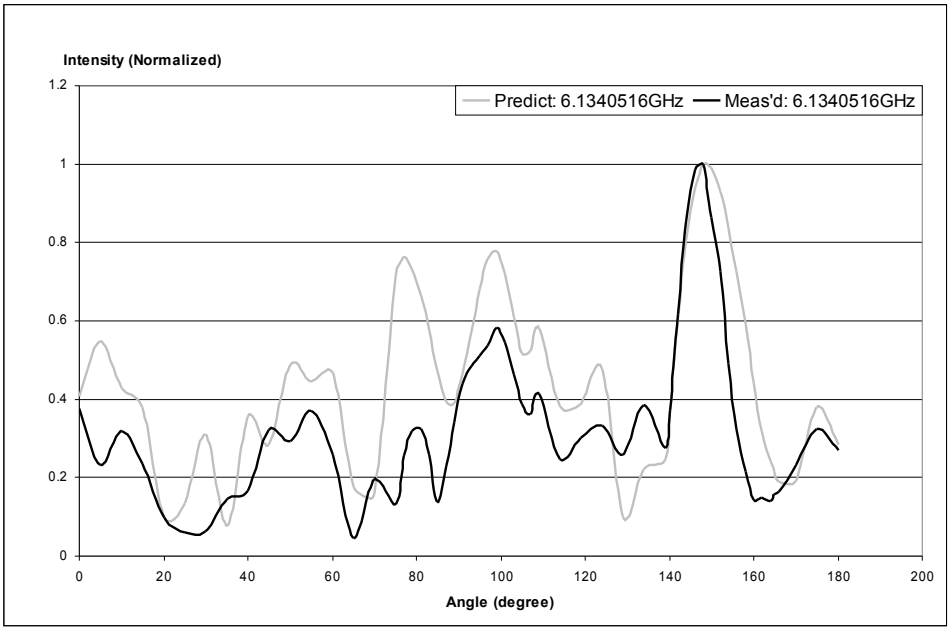

Figure 6.8 - A plot with average deviation from the HFSS model

The return loss for the case of average deviation from the HFSS simulation is shown in Fig. 6.9. Ideally this plot should be flat, as the return loss at one frequency should remain constant across all angles measured. It can be seen at around 100 degrees that the return loss suddenly jumps up. This is consistently the case across all return loss measurements for all frequencies. The reason is that the N-type to SMA adapter was intermittent, and was in the worst position at 100+ degrees.

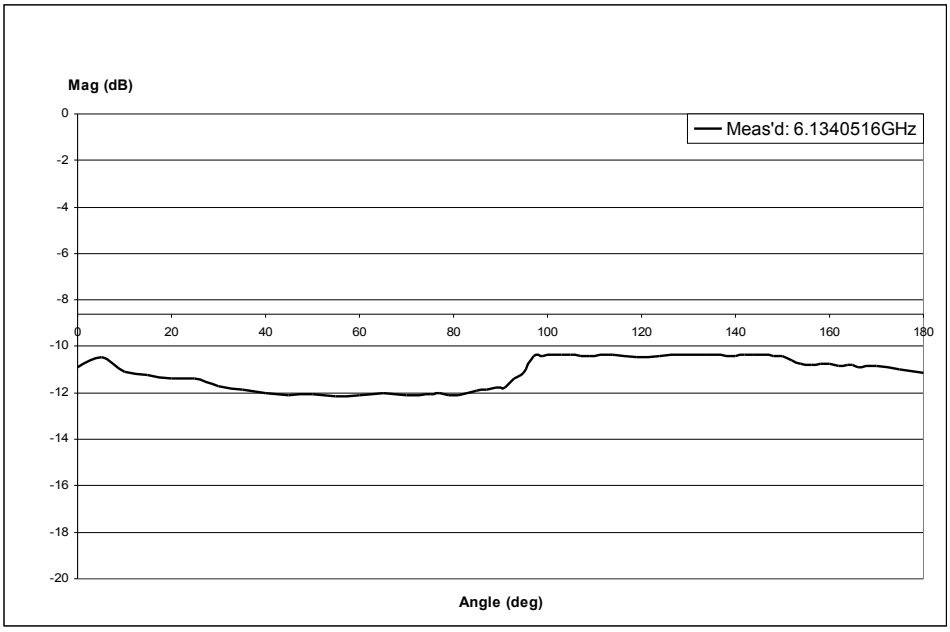

Figure 6.9 - The return loss for the case of average deviation

Overall, the measured data and HFSS simulated data agreed reasonably well. In every graph, one of the two maximum points is near 150 degrees, the diffracted beam. Almost all graphs have the next largest peak at the undiffracted beam location, 100 degrees. Also, in many of both the simulated and measured patterns there is a null at around 160 degrees.

On the other hand, the other features of the graphs (at angles other than 100 degrees or 150 degrees) don't match up too well. Additionally, the return loss, measured over frequencies, Fig. 6.10, does not appear to match up. If, however, the experimental return loss data is shifted, Fig. 6.11, the graphs appear to match reasonably well. It was initially suspected that this shift was due to the location (0.5 inches from the shorting plate – see Section 5.2.1) of the exciting center pin in the HFSS model varying from that

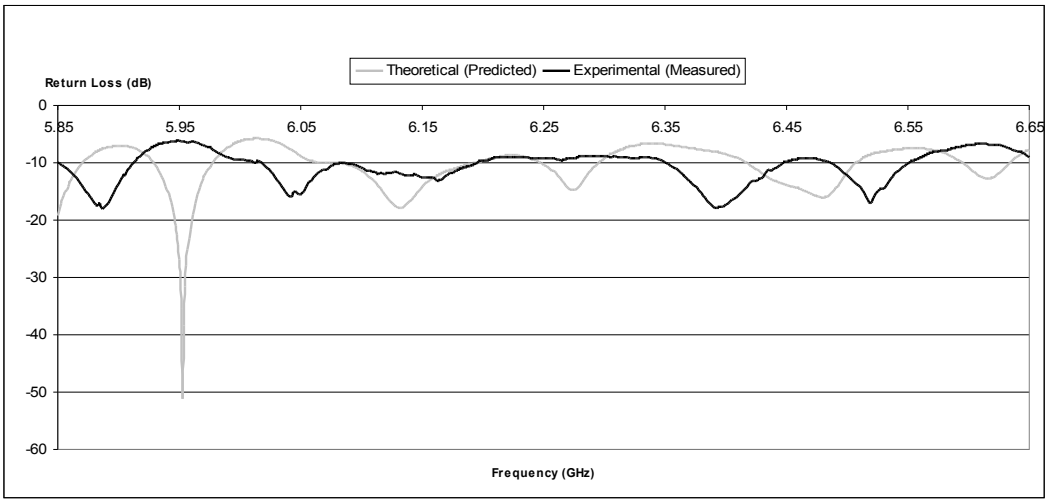

Figure 6.10 - HFSS simulated return loss and measured return loss, best match

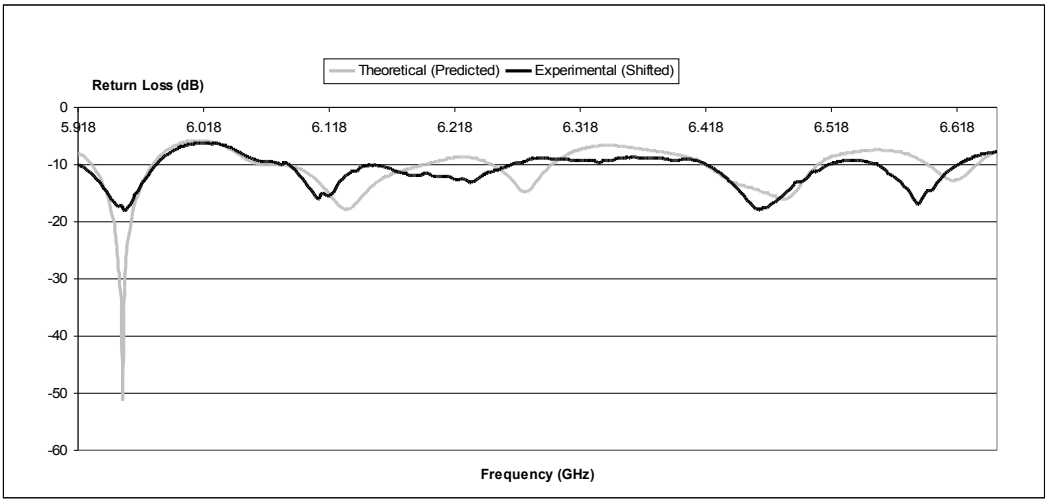

Figure 6.11 - Return loss, experimental data shifted to show matching of qualitative behavior

of the prototype antenna. However, simulation showed that this was not the problem. It might be explained by the intermittent N-type to SMA adapter.

There were some shortcomings of the experimental setup which might explain the discrepancies between the measured and simulated data. The CATR, while having RF absorbing foam blocks, was not the same idealized setting as the HFSS simulation. Also, the best radiation patterns did not occur at the lowest return loss, which indicates that improvements can be made to the waveguide to coax transition. The physical antenna had deformities which the HFSS model did not account for, such as slightly warped sheet metal, extra screw holes above the exciting center pin (originally intended for tuning), or a screw sticking slightly into the rectangular tubing at its interface with the horn section. Additionally, while every attempt was made to make the receiving WR137 antenna and the prototype antenna coplanar, the plane of measurement was not perfectly aligned and horizontal.

Besides radiation patterns, another way in which the simulated and measured data can be compared is by looking at how the location of the diffracted peak changes with frequency (see Section 4.3.1 above). The plot of Fig. 6.12, below, shows that as frequency increases, the location of the Bragg peak shifts lower. The simulated data, experimental data, and Bragg's Law all show the same downward trend. Furthermore, the difference between maximum and minimum angle for both simulated and experimental data is 8 degrees, and for Bragg's Law it is 7.9 degrees, showing excellent agreement.

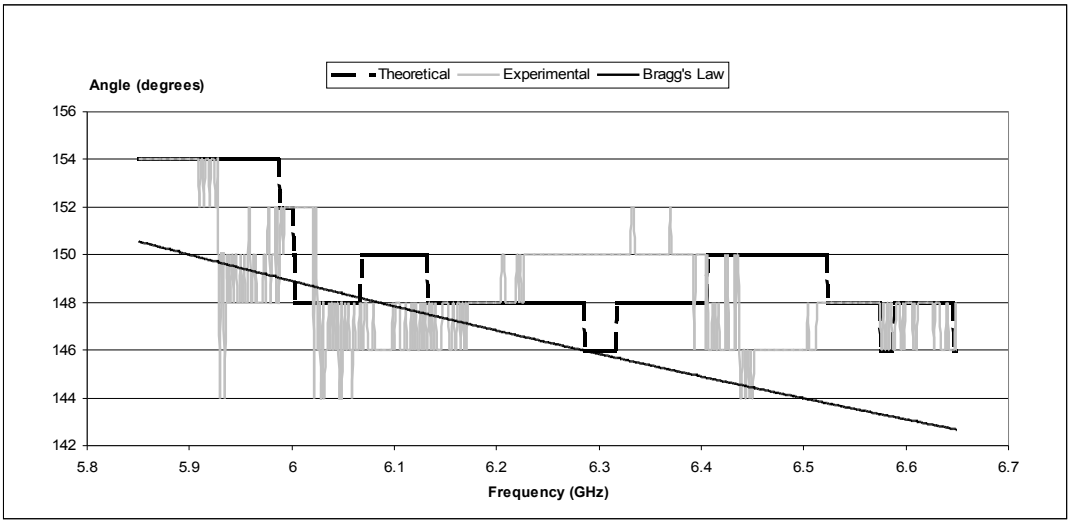

Figure 6.12 - Diffracted peak angle vs frequency: simulated, experimental, and Bragg's Law

As mentioned in Section 4.3.2 the Scherrer equation (4.3) can be recast in frequency dependent form:

$$B(2\theta) = \frac{K\lambda}{L\cos\theta} = \frac{Kc}{Lf\cos\theta} \quad (6.3).$$

Thus as frequency increases, the peak width steadily decreases. The peak width was found by determining the width of the diffracted power peak (or square of the radiation patterns) at each frequency. The best fit value for K was obtained for the data. The plot is shown in Fig. 6.13, and a summary of the pertinent parameters is given in Table 6.3.

The dashed line is the linear fit to the experimental data and shows the expected downward trend. The light gray line is the best fit of the data to the Scherrer equation, obtained by varying K.

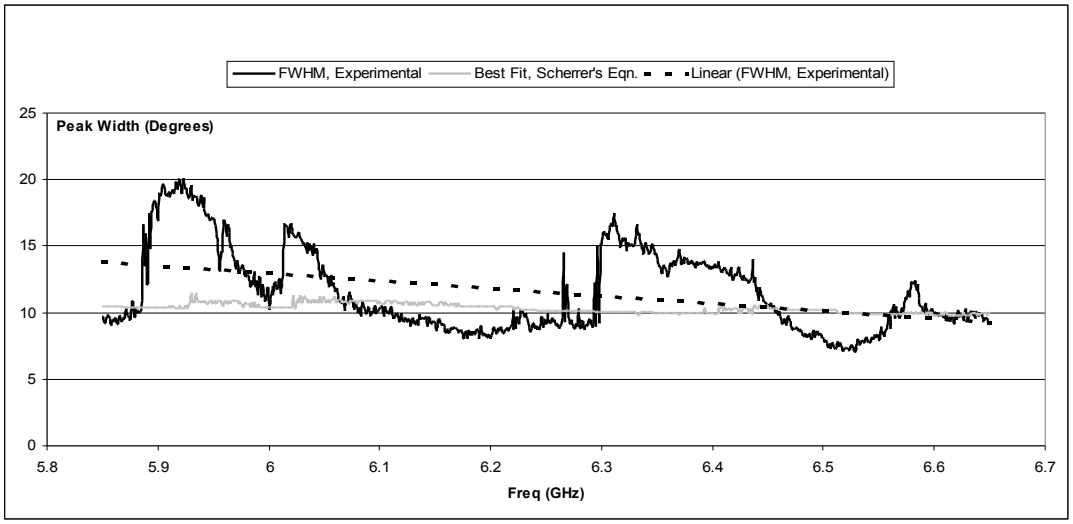

Figure 6.13 - Verification of the Scherrer equation with experimentally determined power peak widths

Table 6.3 - Experimental determination of the shape factor.

K	0.773
L	9.5"
f	swept
θ	experimentally determined diffracted peak

On examination of the above plot, it can be seen that there are frequency ranges where the peak width jumps up. This is due to another peak, next to the diffracted peak, that makes it impossible to determine the true width of the diffracted peak.

The above data confirm that Bragg's Law is indeed at work in predicting the location of the diffracted beam. The radiation patterns show the prominent peak near 150 degrees in all of the radiation patterns measured and the variation of the peak's location

over frequency shows a downward trend – both phenomena predicted by Bragg's Law. The Scherrer equation is qualitatively confirmed in that the peak becomes sharper as the frequency increases.

6.2.2 Best Performance Results

Now that the simulations and measured data have been compared, the best performance radiation patterns will be considered. As a baseline, the radiation pattern of a WR137 waveguide to coax adapter was measured (i.e. both receive and transmit antennas were WR137 adapters). The pattern is given in Fig. 6.14, below. The maximum gain obtained with this antenna was at around 90 degrees, with a gain of -50.405 dB.

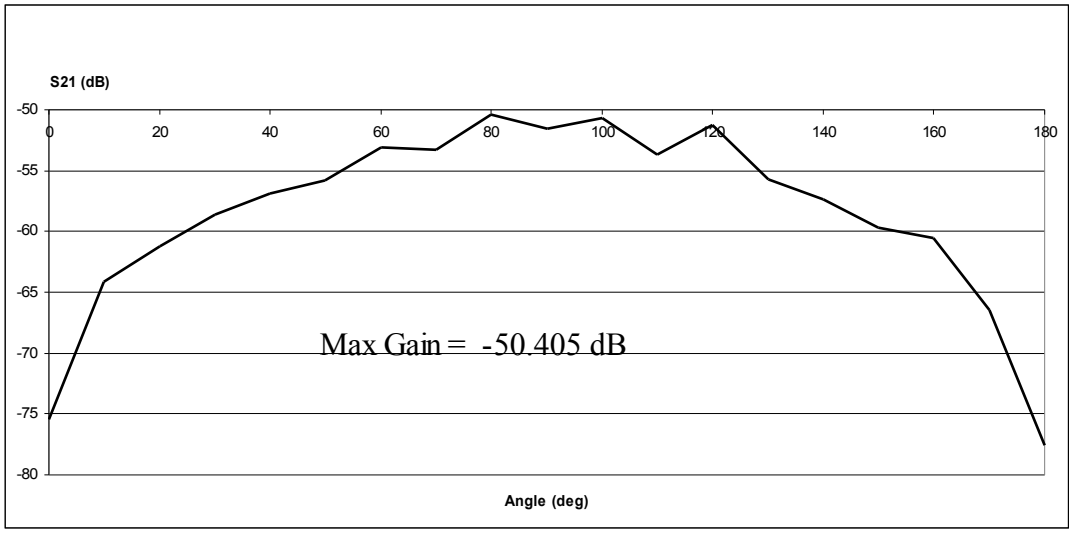

Figure 6.14 - Reference pattern - WR137 open waveguide antenna

There are two best performance cases considered here: the highest gain obtained with the prototype antenna, and the lowest side lobe level between the diffracted and undiffracted beams. In Fig. 6.15 the linear and dB scale graphs of the former case are

shown. In Fig. 6.16 the linear and dB scale graphs of the latter case are shown. Tables 6.4 and 6.5 show the respective antenna parameters for each of these cases. Note that the cross polarization measurement was performed for the 90 degree direction.

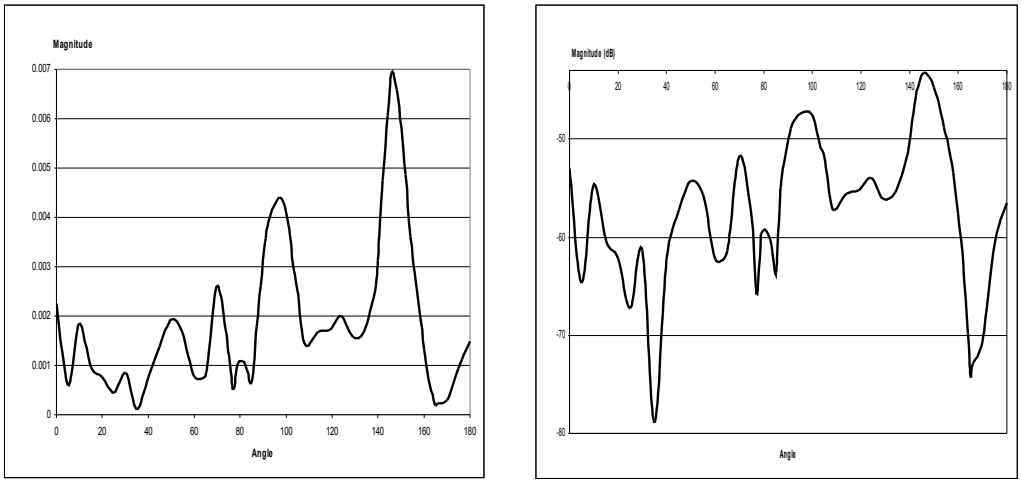

Figure 6.15 - Best performance - highest gain pattern - Left: linear scale; Right: logarithmic scale

*Table 6.4 - Best performance - highest gain pattern *Half power beamwidth*

Freq.	6.083GHz
Max gain	-43.188 dB
Side lobe level	3.949 dB
Gain over waveguide antenna (WR137)	7.217 dB
HPBW*	9.731 degrees
Cross polarization	29.137

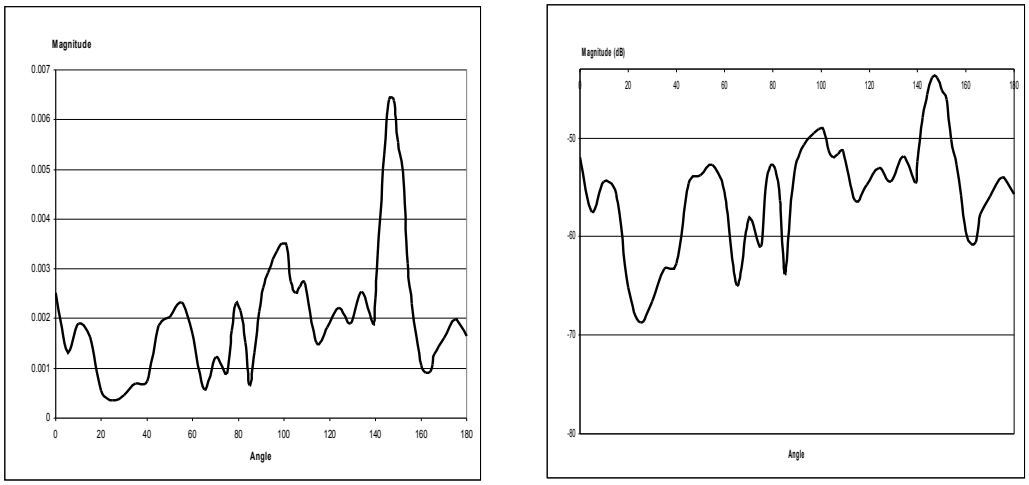

Figure 6.16 - Best performance – lowest side lobe pattern - Left: linear scale; Right: logarithmic scale

*Table 6.5 - Best Performance - highest gain pattern *Half power beam width*

Freq.	6.136GHz
Max gain	-43.876 dB
Side lobe level	5.214 dB
Gain over waveguide antenna (WR137)	6.529 dB
HPBW*	9.845 degrees
Cross polarization	22.186 dB

6.2.3 Near Diffraction Incidence

To further verify Bragg's law another simulation was run. The structure of Fig. 5.13 was used. The diffraction condition for this model occurred at 30 degrees, and the crystal was rotated from this angle by an amount $\Delta\theta$. Table 6.6 shows that the angle of

incidence decreases and the angle of diffraction increases so that the angle of diffraction remains constant. Fig. 6.17 demonstrates that as the deviation from the Bragg condition increases, the diffracted peak magnitude decreases.

Table 6.6 - Near diffraction angle of incidence

Δθ	Angle of incidence	Angle of diffraction	Observed Peak location
0	30	30	60
1	29	31	60
2	28	32	60
3	27	33	60
4	26	34	60
5	25	35	60

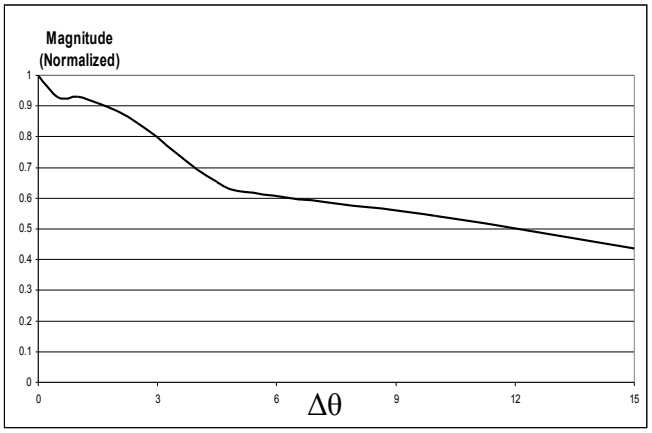

Figure 6.17 - Near diffraction peak magnitude

6.3 Switched Beam Antenna

The results of simulating the structures of Figs. 5.19a and 5.19b (from Section 5.2.3) are given below. The radiation pattern of Fig. 6.18a corresponds diffraction along the +x direction, and the radiation pattern of Fig. 6.18b corresponds to diffraction along

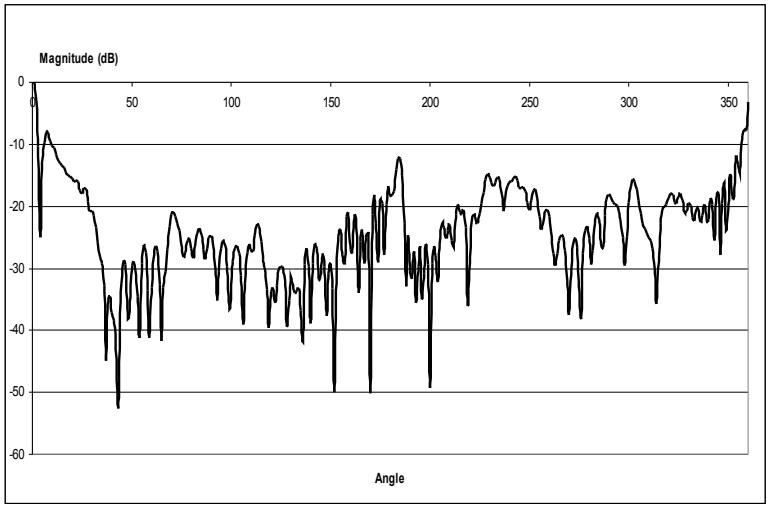

(a) Diffraction along the +x direction

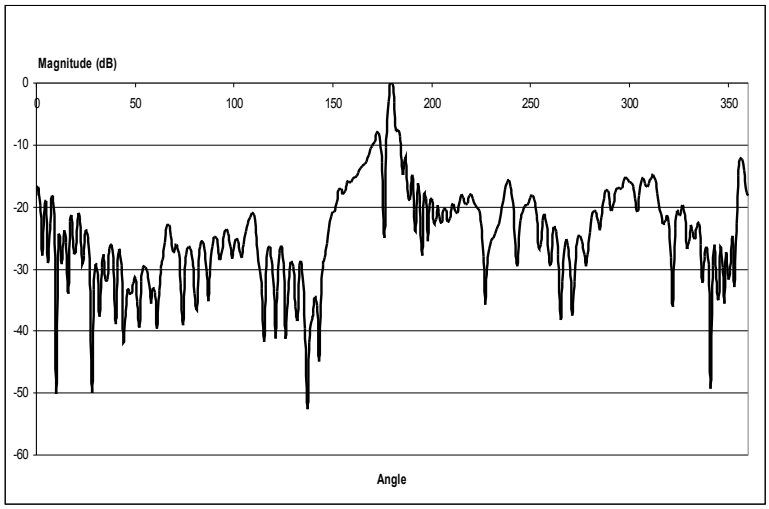

(b) Diffraction along the -x direction
Figure 6.18 - Radiation patterns in dB

the -x direction. For both of these radiation patterns, a rectangular array (i.e. the primary array plus one of the secondary arrays) is used, as in Fig. 5.19. As discussed in Section 4.7.2 analysis of these structures with the Ewald sphere shows that only one diffracted

beam will be present, and in both plots this is observed to be the case. In Fig. 6.18a, there is only one beam, along the 0 degree direction. In Fig. 6.18b, there is only one beam, along the 180 degree direction. The three dimensional linear scale polar plot, super-imposed on the antenna model, is shown in Fig. 6.19. Here it is seen that the main beam of the radiation pattern does indeed go in the -x direction, as in Fig. 6.18b. A plot of the

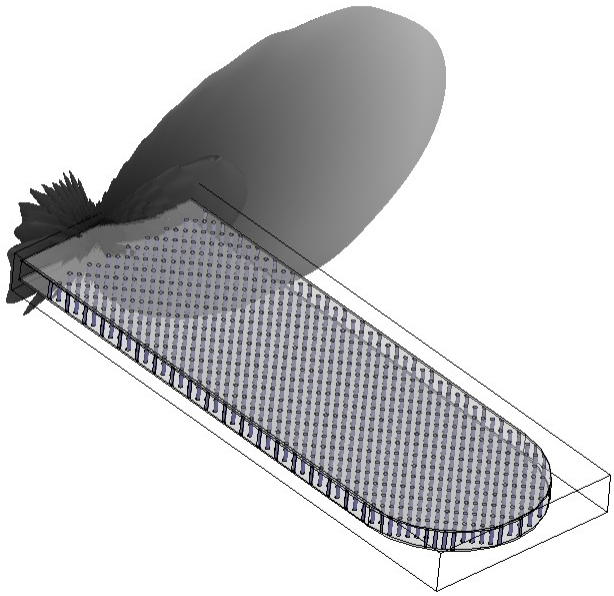

Figure 6.19 - Three dimensional polar plot, super-imposed on the antenna coordinate system, rectangular array

electric field inside of the parallel plate waveguide for the -x diffraction is shown in Fig. 6.20. A summary of the performance results is given in Table 6.7.

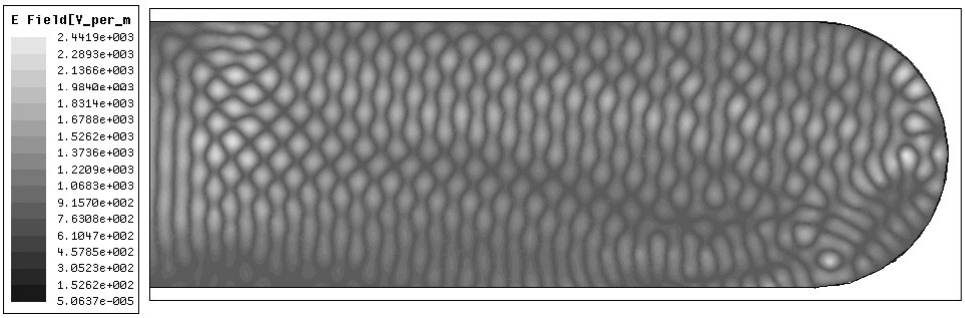

Figure 6.20 - The magnitude of the electric field within the parallel plate waveguide

Table 6.7 - Performance results for the rectangular array, ***-x*** *diffraction*

Freq.	24GHz
Side lobe level	-8.04 dB
HPBW	2-3 degrees
Location of maxima	180 degrees
Number of maxima	1

For the case of the square (or primary) array of Fig. 5.18b, as shown in the discussion on the Ewald sphere, two diffraction maxima are predicted. This is observed in Fig. 6.21, with both maxima at 0 and 180 degrees displayed. The corresponding plot with three dimensional polar plot superimposed on the antenna coordinate system is given in Fig. 6.22. A summary of the performance results for the primary array is given in Table 6.7.

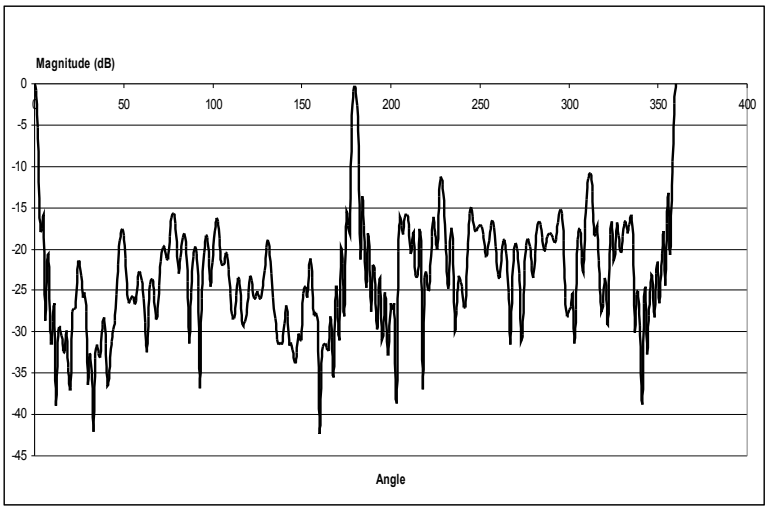

Figure 6.21 - Square (or primary) array radiation pattern

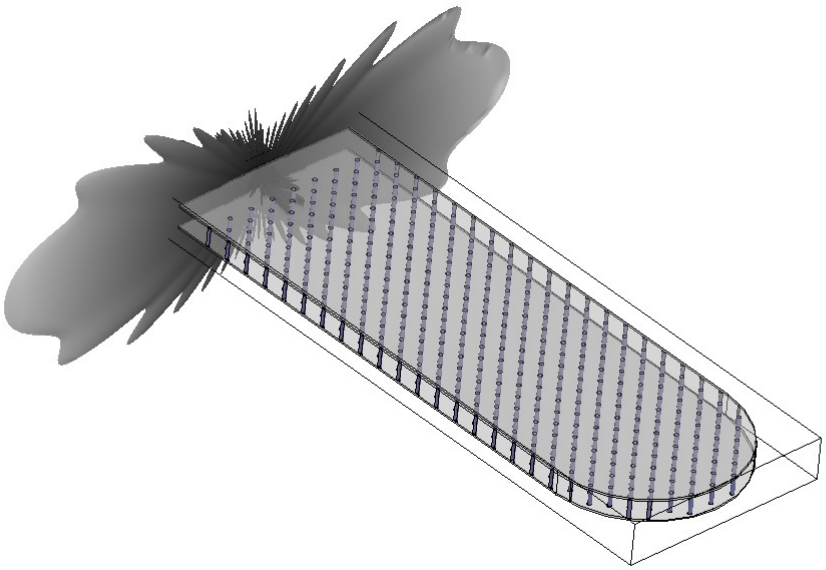

Figure 6.22 - Three dimensional polar plot, super-imposed on the antenna coordinate system, square (or primary) array

Table 6.8 - Performance results for the square (primary) array

Freq.	24 GHz
Side Lobe Level	-15.72 dB
HPBW	2-3 degrees
Location of Maxima	0, 180 degrees
Number of Maxima	2

For this switched beam design, there are three possible configurations: a main beam along the +x direction, the -x direction, or in both the +x and -x directions. For all three configurations, the HPBW is essentially the same. However there is a trade-off between the location of the maxima and the side lobe level. While the +x and -x direction patterns are desirable in that only one beam is present, the side lobe level goes from 15 dB to 8 dB, a significant, although not unacceptable increase.

At this point it is worth noting a quality of the switched beam design that is slightly different from that of the prototype antenna – the location of the undiffracted beam. For simulations having metal posts the undiffracted beam comes out at an angle other than 90 degrees. In the measurement of the prototype antenna, for example, the undiffracted beam was at 100 degrees. It was also observed in simulations that as the distance between metal posts within a plane was decreased the undiffracted peak tended to move away from 90 degrees, approaching $\theta_{Bragg} + 90$ degrees. The beam stop will not effectively shield the undiffracted beam for designs with metal posts, since the undiffracted beam will exit the parallel plate structure at an angle other than 90 degrees.

The reason the beam stop was useful for the switched beam design discussed here is that the undiffracted beam is at 90 degrees.

In X-ray diffraction experiments, as with the dielectric post designs discussed here, the undiffracted beam is always at 90 degrees. From this observation, it can be inferred that the analogy between an X-ray impinging on a crystal of atoms and an RF beam impinging on an array of dielectric posts is the most accurate. Metal provides a "harder" target for the RF beam than an electron cloud provides for an X-ray beam, and as a result, the undiffracted beam strays from the expected 90 degrees.

7. CONCLUSION AND FURTHER WORK

7.1 Conclusion

Various principles of X-ray crystallography have been verified at radio frequency, using software simulations. Furthermore, these principles can be used to tailor specific parameters in an antenna design. The antenna array size, along with the angle of incidence relative to a plane of posts, determines the HPBW of the antenna: the longer the antenna array, the sharper the peak, and the higher the angle, the wider the peak. This is described via the Scherrer equation. Using Bragg's Law, the direction of the main lobe can be determined. Ewald Sphere formalism can be used to design a switched beam antenna, predicting what the direction of the main lobe will be for a given antenna array configuration. The validity of these laws at RF show that the theory of X-ray diffraction can be applied to design antennas.

Additionally, a model was constructed and tested at RF as a means of further verifying the principles of X-ray crystallography at radio frequencies. The data taken from the antenna constructed showed that Bragg's Law effectively predicted the location of the main lobe and also showed that the dependence of the HPBW over frequency followed the Scherrer equation. The antenna's best performance occurred at 6.136GHz, and showed a grating lobe at 5.2 dB less than the main lobe and a gain of 6.5 dB over a rectangular waveguide.

7.2 Further Work

7.2.1 Improved Antenna Design

There are several ways in which the antenna design could be improved. First, the feed structure, an H-plane horn, could produce a higher quality plane wave by using a fast-lens antenna. The fast lens would be inserted into the parallel plate section just after the H-plane horn. The fast lens would be used as a diverging lens, with its focal point somewhere inside the H-plane horn. The overall effect would be to "speed up" the edges of the wave, so that it becomes more planar when it impinges upon the array of posts. This would improve the HPBW, decrease the grating lobe level, and increase the intensity of the main lobe.

Second, the interaction length of the antenna could be increased. If the antenna array was increased in length, then the diffracted beam would be stronger and have a decreased HPBW.

Finally, an SMA feed could be used in the waveguide to coax adapter section to eliminate the need for an N-type-to-SMA adapter. This would improve the return loss measurement.

7.2.2 Electrically Tunable Antenna

A proof of concept for a tunable antenna could be demonstrated by constructing the antenna model of Section 5.2.3 using the improve feed structure discussed above. As a post material, Delrin could be used, since it has a dielectric constant close to that used

in the model. The parallel plate section would have a semicircle shape at the end (as in the model of Fig. 5.18). There would also be a beam stop along the curved opening on the end of the parallel plate section. To change the direction of the diffracted beam, sets of posts could be removed and replaced and the radiation pattern measured each time.

7.2.3 Non-Simple Arrays

In this paper, only square or rectangular arrays of posts were used, as they are the simplest. More complex arrays, such as a diamond-shaped array or an array with imperfections introduced, could be explored. The goal of such an exploration would be to determine arrays that could yield the largest number of beam directions for the fewest of posts.

REFERENCES

[1] M. Woolfson, *An Introduction to X-ray Crystallography*, 2nd ed., Cambridge: Cambridge Univ. Press, 1997, p. 108.

[2] W. L. Bragg, "The diffraction of short electromagnetic waves by a crystal," *Proc. Cambridge Philos. Soc.*, vol. 17, pp. 43–57, 1913.

[3] P. Scherrer, “Göttinger nachrichten,” *Math. Phys*, vol. 98, 1918.

[4] E. Yablonovitch, “Inhibited spontaneous emission in solid-state physics and Electronics,” *Phys. Rev. Lett.*, vol. 58, no. 20, pp. 2059–2062, 1987.

[5] J.M. J. Danglot, O. Vanbesien, D. Lippens, et al, “Toward controllable photonic crystals for centimeter and millimeter wave devices,” *J. Lightw. Technol.*, vol. 17, no. 11, 1999.

[6] E.R. Brown, C.D. Parker, E. Yablonovitch, “Radiation properties of a planar antenna on a photonic crystal substrate,” *J. Opt. Soc. Am.,* B10, 404-407, 1993.

[7] O. Vanbesien, J. Danglot, D. Lippens, “A smart K-band four port resonant switch based on photonic band gap engineering.” *29th Euro. Microwave Conf.*, Munich 1999.

[8] J. Carbonell, O. Vanbesien, D. Lippens, “Electric field patterns in finite two-dimensional wire photonic lattices,” *Superlattice Microst*, vol. 22, no. 4, 1997.

[9] Chang, I.C.; , "Intermodular products in phased array Bragg cells," *Ultras. Symp., Proc., IEEE*, pp.505-508 vol.1, 3-6, 1989.

[10] G. von Freymann, et al; "Angle- and spectrally-resolved Bragg scattering on two-dimensional silicon-based photonic crystals," *Quantum Electronics and Laser Science, QELS. Postconf. Digest.*, pp. 1-6, 2003.

[11] H. Tsuchiya, N. Lertsirisopon, M. Ghoraishi, J. Takada, T. Kobayashi; "Influence of Bragg scattering on UWB signal reflection from a periodic surface," in *Proc. IEICE Gen. Conf. (Inst. Elect., Inform. Comm. Eng.)*, pp17-18, 2006.

[12] R. Vaughan, "Switched parasitic elements for antenna diversity," *IEEE Trans. on Ant. and Propag.*, vol. 47, no. 2, pp. 399-405, 1999.

[13] J. B. Keller, "Geometrical theory of diffraction," *J. Opt. Soc. Am.*, vol. 52, no. 2, pp. 116-130, 1962.

[14] F. Molinet, "Geomatrical theory of diffraction (GTD) Part I: Foundation of the theory," *IEEE*, vol. 29, no. 4, pp. 6-17, 1987.

[15] F. Molinet, "Geometrical Theory of Diffraction(GTD) Part II: Extensions and future trends of the theory," *IEEE*, vol. 29, no. 5, pp. 5-16, 1987.

[16] C.A. Balanis, *Antenna Theory: Analysis and Design, 3rd Edition*, Wiley-Interscience, 2005, pp. 740, 742, 756.

[17] D. Pozar, *Microwave Engineering*, Hoboken NJ: Wiley, 2005, pp. 105, 113.

[18] B. Warren, *X-ray Diffraction*, Reading Mass.: Addison-Wesley Pub. Co., 1969, pp. 16, 18, 31, 251-254.

[19] A. L. Patterson, "The Scherrer formula for X-ray particle size determination," *Phys. Rev.*, vol. 56, no. 10, pp. 978–982, 1939.

APPENDIX - Ansoft HFSS Software

The worked presented in this paper relies heavily on the Ansoft HFSS software for verification of the crystallographic laws presented, as well as the design of an actual antenna prototype. It is therefore worthwhile to discuss the theoretical aspects of the software, as well as the core functionality.

Ansoft HFSS is a three-dimensional full-wave solver that uses the finite element method. In simulating a design, the following steps must be completed:

1. Create a 3D model of the device of interest. Most designs can be constructed using fundamental geometric shapes such as spheres, boxes, cylinders, etc. – all of which are available in the HFSS interface. Two-dimensional shapes may be drawn as well and they can be swept along vectors, or rotated around an axis, to create 3D objects. The basic operations of geometry are available, as well as "Boolean" operations, where, for example, objects can be united or split apart. [Required]

2. Set the boundary conditions. The electromagnetic boundaries must be set up. Surfaces of shapes can be set to be either electric boundaries ("perfect E"), or magnetic boundaries ("perfect H"). Also, materials can be assigned to 3D objects; the appropriate boundary conditions for that material, as well as its bulk properties (conductivity, permittivity, etc.) are automatically accounted for in the calculations. [Required]

3. Set the excitations. In order for the design to be analyzed, energy must enter the design in some part of the design. This is usually a wave port being fed into a waveguide of some kind. There are different types of stimuli available for different structures, however. For all of the designs in this work, the wave port is the stimulus. [Required]

4. Analysis setup. This sets the frequency of the excitation, as well as the convergence criterion. [Required]

5. Post processing. This step is optional. As the name implies, it is for calculations that may be done after the structure has been solved. The steps may be completed ahead of time so that the calculations can be done immediately following the structure's solution.

In Fig. A.1 below, an example is shown of the validation for a specific design. Some of the steps are optional, such as the Radiation (for finding far field or near field characteristics) and optimetrics (for simulating structures that have a varying parameter).

To solve a structure, the software creates a mesh of tetrahedra that fill the volume of the interest. The Maxwell equations are then solved numerically at each point in the mesh, and the electric and magnetic fields are known. Additional information, such as S-parameters and antenna characteristics, can also be found in the post-processing,

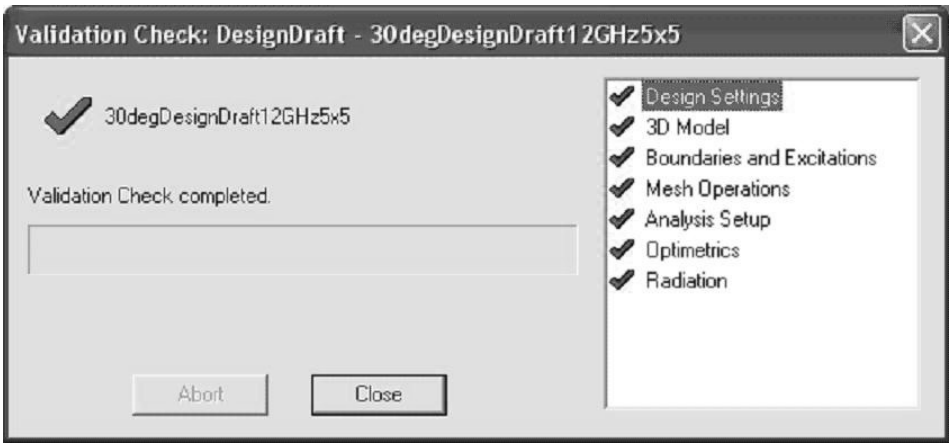

Figure A.1 - The basic components of the HFSS software

The setup of the radiation calculations is common to all of the designs in the present work. To do this, two steps are necessary. First, set up a coordinate system specifying all of the directions for which the radiation data is desired. Second, specify the desired graph, such as a radiation pattern or a 3D polar plot. After the structure is solved, the report is automatically updated.